3rd AIAA Flow Control Conference
5 - 8 June 2006, San Francisco, California

AIAA 2006-3340

Some Detailed Information of a Low Speed Turbulent Flow over a Bluff Body Evaluated by New Time-Frequency Analysis

Yih Nen Jeng [*] and Jr Chi-Tsung Chen[†]
Department of Aeronautics and Astronautics, National Cheng Kung University
Tainan, Taiwan 70101, Republic of China

You-Chi Cheng [‡]
Department of Electrical Engineering, National Taiwan University
Taipei, Taiwan, 101, Republic of China

Time varying $u-$velocity data measured at the wake region of a low speed flow over a bluff body are shown to have the turbulent characteristics via the Hurst analysis. By using a diffusive iterative filter, these data are decomposed into smooth and high frequency parts, respectively. Spectrums with small errors of these high frequency parts are subsequently evaluated. Gaussian window centered at a given frequency is employed to weigh a spectrum and hence the corresponding band-pass limited data is obtained. The enhanced Morlet transform uses these band-pass limited data instead of employing the original data. The resulting two-dimensional wavelet coefficient plot clearly shows many detailed information and overall features of the flow field: such as the frequency shift of a waveform, the merging between waveforms with their frequencies close to each other, how a waveform starts and terminates, etc. The modified Hilbert transform is employed to calculate amplitudes and frequencies of the shedding frequency and several sub-harmonic waveforms. A quantitative study of these waveforms shows some information of the energy cascade between them such that, in the wake region, the shedding frequency waveform releases energy to other waveforms and the flow field contains the low frequency modulation.

Nomenclature

A	=	attenuation factor of iterative filter, amplitude
a	=	attenuation factor, scale function of the Morlet transform
B	=	constant
b	=	Fourier coefficient
c	=	Fourier coefficient, Hermite interpolation coefficients, and window size factor
d	=	second order derivative
f	=	frequency
H	=	Hurst exponent
i	=	time or spatial index
J	=	modified Hilbert transform of x
k	=	constant, mode number
m	=	iteration number
N	=	data number
n	=	mode index
L	=	mode index
p	=	high order slope
R	=	departure estimation
S	=	sample deviation

[*] Professor, Dept. of Aero. & Astro., National Cheng Kung University, Tainan, Taiwan, R.O.C., AIAA Member. Email: z6208016@email.ncku.edu.tw
[†] Ph. D. Candidate, Dept. of Aero. & Astro., National Cheng Kung University, Tainan, Taiwan, R.O.C..
[‡] Bachelor, Dept. of Electrical Eng., National Taiwan University, Taipei, Taiwan, R.O.C..

s = slope, first order derivative
T = sampling range
t = time, second order derivative
U_0 = mean velocity at inlet of the wind tunnel
u = velocity
W = wavelet coefficient
x = data
X = rescaled time span
y = data
z = complex data
Δt = time interval
ξ = data
λ = wavelength
σ = factor of Gaussian function
θ = phase angle
τ = time

I. Introduction

After the work about the low frequency unsteadiness of Bloor [1], many studies on the low-frequency variations embedded in the vortex shedding process have been followed. Miau et al. [2-4] had preformed extensive studies upon the detailed structures and mechanisms of the vortex shedding at a low Reynolds number. In Ref.[5-10], Miau et al. studied the low frequency modulation for flows over different configurations of bluff bodies in different ranges of the Reynolds numbers. In these studies, both the Morlet transform [8-10] and empirical mode decomposition method [7] were successfully employed.

In order to study the complicated flow field in the wake region, Ref.[7] employed the empirical mode decomposition method and got many valuable insights. Since the method of the empirical mode decomposition is principally based on an average between the upper and lower envelopes of a data string, it cannot arbitrarily control the frequency bandwidth of a waveform. As a consequence, the extracted turbulent characteristics do not contain many detailed information [7]. In Ref.[15-16], the Morlet transform is enhanced by introducing a band-pass limited data for every scale function of the transform and using a diffusive iterative filter [17-20]. The band-pass limited data are obtained via a simple strategy of employing a Fast Fourier Transform (FFT) [21] together with the diffusive iterative filter. As compared with the result of the original method, a clearer picture of the time-frequency feature is gotten [15-16]. In order to examine the energy flow in and flow out of a waveform, the modified Hilbert transform [13, 14, 22, 23] will be employed in this study to find the amplitude and frequency of a band-pass limited data string correctly.

In early days, people recognized that a turbulent flow is related to the random processes [24,25]. One of these studies is the Hurst analysis [26]. In 1962, Lamperti [27] proved the self-similar theorem of a random process. Later Mandelbrot [28] pointed that the self-similar property can be properly interpreted by the fractal analysis such that the Hurst analysis can be employed to identify a random process. This study will employed the Hurst analysis to make sure that the flow field studied in Ref.[4-6] is turbulent.

II. Analysis

Hurst Analysis [26]

Assume that a time series data string $\xi_i = \xi(i\Delta t)$, $i = 0,1,...,N$ is known. The average of the rescaled time-span, $\langle \xi \rangle_\tau$, where $0 < \tau \le N\Delta t$, is defined as

$$\langle \xi \rangle_\tau = \frac{1}{\tau}\sum_{i=0}^{N} \xi_i \tag{1}$$

The accumulated departure of the rescaled time-span $X(t',\tau)$, where $t' \le \tau$, is defined as follows.

$$X(t',\tau)=\sum_{j=1}^{\tau}\left(\xi_j-\langle\xi\rangle_\tau\right) \tag{2}$$

Subsequently, the departure estimation $R(\tau)$ and sample deviation $S(\tau)$ are defined in the following equations, respectively.

$$R(\tau)=\max\left[X(t',\tau)\right]-\min\left[X(t',\tau)\right] \tag{3}$$

$$S(\tau)=\left[\frac{1}{\tau}\sum_{t'=\Delta t}^{\tau}\left[\xi(t')-\langle\xi\rangle_\tau\right]^2\right]^{1/2} \tag{4}$$

The normalized departure is defined as R/S. Hurst pointed that the exponent H in the following relation is related to the random process.

$$R/S=(k*\tau)^H \tag{5}$$

where k is a constant. If $H=1$, the data string is smooth and carries a deterministic behavior. The random nature is more and more obvious as H becomes smaller and smaller. There are three different values of the Hurst exponent which are corresponding to three kinds of system status in the region of $0<H<1$, respectively.

1. The case of $H=0.5$ means that the experimental system appears in a random tendency and stays in the state of a classic Brownian motion.
2. When $H<0.5$, it indicates that the system is a fractional Brownian motion and appears an anti-persistent status.
3. When $1>H>0.5$, it means that the system has a high fractional Brownian motion and appears a persistent status which may or may not be properly predicted. It also means that the time series system partially repeats itself rather than in a fully random procedure. Since a turbulent flow is not a fully random process, it belongs to this category.

Data of these three systems are referred to as the white, pink, and black noises, respectively.

The Iterative Filter Based on Gaussian Smoothing

Assume that a discrete data string can be approximated by

$$y(t)=\sum_{n=0}^{N}\{b_n\cos\left(\frac{2\pi t}{\lambda_n}\right)+c_n\sin\left(\frac{2\pi t}{\lambda_n}\right)\} \tag{6}$$

where $\lambda_n=T_{total}/n$. In Ref.[17-20], it was proven that, after applying Gaussian smoothing method once, the resulting smoothed data becomes

$$\bar{y}_1(t)\approx\sum_{n=0}^{N}a(\sigma/\lambda_n)\{b_n\cos\left(\frac{2\pi t}{\lambda_n}\right)+c_n\sin\left(\frac{2\pi t}{\lambda_n}\right)\} \tag{7}$$

where $a(\sigma/\lambda_n)$ is the attenuation factor introduced by the smoothing procedure. It can be proven numerically that

$$0\le a(\sigma/\lambda_n)\approx\exp[-2\pi^2\sigma^2{\lambda_n}^2]\le 1 \tag{8}$$

If the high frequency part is repeatedly smoothed by Gaussian smoothing method, the result at the $m-$th step is

$$y_m^{'}=\sum_{n=0}^{N}[1-a(\sigma/\lambda_n)]^m\left[b_n\cos\left(\frac{2\pi t}{\lambda_n}\right)+c_n\sin\left(\frac{2\pi t}{\lambda_n}\right)\right]$$

$$\bar{y}(m)=\bar{y}_1+\bar{y}_2+\ldots+\bar{y}_m=y-y_m^{'}=\sum_{n=0}^{N}A_{n,m,\sigma}\left[b_n\cos\left(\frac{2\pi t}{\lambda_n}\right)+c_n\sin\left(\frac{2\pi t}{\lambda_n}\right)\right] \tag{9}.$$

where $y_m^{'}$ and $\bar{y}_m$ are the high frequency and smoothed parts at the $m-$th smoothing step, respectively. Finally, $\bar{y}(m)$ is the desired smooth part and $y_m^{'}$ is the high frequency part. Obviously, both the original Gaussian smoothing and iterative smoothing algorithms are diffusive.

Suppose that all the waveforms within the range of $\lambda_{c1}<\lambda<\lambda_{c2}$ are insignificantly small. By using $0.5(\lambda_{c1}+\lambda_{c2})$ as a cutting point, the above mentioned iterative smoothing procedure is an effective filter to give both

the low and high frequency parts [17-20] without introducing any dispersive error. The desired parameter σ and number of iteration steps m are solved by the following simultaneous equations.

$$A_{c1,m,\sigma} = 1-[1-\exp(-2\pi^2\sigma^2/\lambda_{c1}^{\ 2})]^m = B_1$$
$$A_{c2,m,\sigma} = 1-[1-\exp(-2\pi^2\sigma^2/\lambda_{c1}^{\ 2})]^m = B_2 \qquad (10)$$

where $B_1, B_2 = 0.001,\ 0.999$, respectively, are employed in this study.

Fourier Spectrum with Small Error

In general, if a Fast Fourier Transform algorithm (FFT) is employed to evaluate the spectrum of a data string consisting of a non-sinusoidal part, the resulting spectrum always shows an exponentially decayed trend. The contribution of the non-sinusoidal part is referred to as the Direct Current (DC) contamination. Consequently, many quantities of the sinusoidal features in the low frequency regime can not be clearly identified. The non-periodic condition introduces a negative contribution, too. In Ref.[21], the cubic moving least squares method was employed to remove the non-sinusoidal part and developed a strategy to further remove the effect of the non-periodic condition. Since the transition zone, $(\lambda_{c1}, \lambda_{c2})$, of the cubic moving least squares method is still too wide, the above iterative filter was employed to remove it and the low frequency part in Ref.[17-20]. Subsequently, a spectrum with small spectrum error can be evaluated via the following procedures.

1. For the remaining high frequency part, choose zero crossing points around the two ends. Use an interpolation method to find the corresponding locations of these 0s. Since the iterative filter can not approximate data very well at the two ends, it is recommended to discard several zeros around the two ends as will be shown in the discussion section.
2. Use the following modified monotonic cubic interpolation [21,29] to redistribute the data, say,

$$y(x) = c_3(x-x_i)^3 + c_2(x-x_i)^2 + c_1(x-x_i) + c_0$$
$$c_0 = y_i,\ c_1 = y_i^{'},\ s_{i+1/2} = (y_{i+1}-y_i)/(x_{i+1}-x_i),\ c_2 = \frac{3s_{i+1/2} - 2y_i^{'} - y_{i+1}^{'}}{x_{i+1}-x_i},\ c_3 = \frac{y_i^{'} + y_{i+1}^{'} - 2s_{i+1/2}}{(x_{i+1}-x_i)^2} \qquad (11),$$
$$y_i^{'} = \mathrm{sgn}(t_i)\min\left[\frac{1}{2}\left|p_{i-1/2}^{'}(x_i) + p_{i+1/2}^{'}(x_i)\right|, \max\left\{k\,|\,s_i\,|, \frac{k}{2}|\,t_i\,|\right\}\right]$$
$$p_{i-1/2}^{'}(x_i) = s_{i-1/2} + d_{i-1/2}(x_i - x_{i-1}),\ p_{i+1/2}^{'}(x_i) = s_{i+1/2} + d_{i+1/2}(x_i - x_{i+1}),$$
$$t_i = \min\mathrm{mod}\left[p_{i-1/2}^{'}(x_i), p_{i+1/2}^{'}(x_i)\right],\ d_{i+1/2} = \min\mathrm{mod}[d_i, d_{i+1}]$$
$$d_i = (s_{i+1/2} - s_{i-1/2})/(x_{i+1} - x_{i-1}),\quad s_i = \min\mathrm{mod}\left[s_{i-1/2}, s_{i+1/2}\right]$$
$$k = 3,\ \text{if } |s_{i+1/2}| >> |s_{i-1/2}|, \text{ or } |s_{i-1/2}| >> |s_{i+1/2}|$$
$$\geq 4,\ \text{otherwise}$$

   and the total number of points is set to be 2^m. For a smooth data string, at least one point should be located in the range between two successive data points of the original data string to reduce the interpolation error. For an oscillatory data such as the turbulent data taken by an insufficient sampling rate, more than 4 points should be considered.
3. Perform an odd function mapping with respect to one end so that the range of the final data is doubled.
4. A simple FFT is employed to generate the desired spectrum.

The odd function mapping makes sure that the periodicity is valid up to the highest order of derivative such that the data can resolve. Consequently, the spectrum error can be effectively reduced. In fact, this transform gives a Fourier sine spectrum.

Enhanced Morlet Transform

For a given data string, the Morlet transform evaluates the wavelet coefficient by the formula [11,12,22].

$$W(a,\tau) = \frac{1}{\sqrt{a}}\int_{-\infty}^{\infty} y(t)e^{-i6(t-\tau)/a}e^{-(t-\tau)^2/(2a^2)}dt \qquad (12)$$

where a is called the scale function of the transform. Basically, it transforms a one-dimensional data string into the two-dimensional (a,τ) plane where a is related to the wavelength or frequency and τ represents the time scale. If the original data is expressed in the form of Eq.(6), the resulting wavelet coefficient is approximated by the following formulas.

$$\overline{W}(a,\tau,y) \approx \sqrt{\frac{\pi a}{2}}\left\{\sum_{n=0}^{\infty} b_n \exp\left(-\frac{a^2}{2}\left[\frac{2\pi}{\lambda_n}-\frac{6}{a}\right]^2\right)\exp\left[\frac{i2\pi\tau}{\lambda_n}\right]+\sum_{n=0}^{\infty} c_n \exp\left(-\frac{a^2}{2}\left[\frac{2\pi}{\lambda_n}-\frac{6}{a}\right]^2\right)\exp\left[-\frac{i2\pi\tau}{\lambda_n}\right]\right\} \tag{13}$$

Obviously, for a given scale function a, the maximum response occurs at $\lambda = 1/f \approx a\pi/3$. A careful inspection of Eqs.(12) and (13) reveals that Gaussian window of the Morlet transform on the time domain results in a band-pass limited spectrum characterized by a corresponding Gaussian window. Moreover, the band-width of the resulting spectrum introduced by Gaussian window is too wide so that the visibility of the resulting wavelet coefficient plot generated by this continuous wavelet transform is not good enough [11,12].

With the help of the iterative filter, the FFT algorithm of Ref.[21] is employed to give the band-pass limited data via the following steps. At first, the iterative filter is employed to remove the non-sinusoidal and low frequency parts. Then, the above mentioned FFT algorithm is used to evaluate the spectrum of the high frequency part with a small error. For a given scale function a, a band-pass limited spectrum is obtained by weighting the spectrum by Gaussian function whose center locates at $\lambda_L = a\pi/3$. A typical example is shown in Fig.1. After the band-pass limited spectrum is obtained, the inverse FFT algorithm is employed to give the following band-pass limited data string for the scale function a.

$$y_L^H(t) = \sum_{n=0}^{N} e^{-(n-L)^2(2\sigma_L^2)}\{b_n \cos\left(\frac{2\pi t}{\lambda_n}\right)+c_n \sin\left(\frac{2\pi t}{\lambda_n}\right)\} \tag{14}$$

where the superscript H designates the high frequency part. This data string is referred to as the $L-$th wave mode corresponding to the frequency $f_L = 1/\lambda_L$. In Eq.(14), σ_L is the window size of Gaussian function on spectrum domain and is determined by the relation

$$\sigma_L = c \cdot \max[|k_L - k_{L-1}|, |k_{L+1} - k_L|] \tag{15}$$

where $k_L = T_{\text{total}}/\lambda_L$ and c is an user defined parameter of window size. Finally, instead of using the original $y(t)$, $y_L^H(t)$ is employed in Eq.(12) to evaluate the wavelet coefficients so that an enhanced version of the Morlet transform is obtained. It can be proven that the resulting wavelet transform converts the high frequency part of the original data string to be

$$\begin{aligned}\overline{W}(a,\tau,y) \approx \sqrt{\frac{\pi a}{2}} \times \Bigg\{ & \sum_{n=0}^{\infty} b_n \exp\left(-\left[\frac{a^2}{2}+\frac{T^2}{8\pi^2\sigma_L^2}\right]\cdot\left[\frac{2\pi}{\lambda_n}-\frac{6}{a}\right]^2\right)\exp\left[\frac{i2\pi\tau}{\lambda_n}\right] \\ & + \sum_{n=0}^{\infty} c_n \exp\left(-\left[\frac{a^2}{2}+\frac{T^2}{8\pi^2\sigma_L^2}\right]\cdot\left[\frac{2\pi}{\lambda_n}-\frac{6}{a}\right]^2\right)\exp\left[-\frac{i2\pi\tau}{\lambda_n}\right]\Bigg\}\end{aligned} \tag{16}$$

Without the extra-window term, the remaining factor $\exp[-a^2(\cdot)/2]$ can not be ignored over a certain band of spectrum.

Modified Hilbert Transform

For a data string $x(t)$, defined in the range of $-\infty < t < \infty$, the following Hilbert transform is the corresponding imaginary part provided that $x(t)$ is sinusoidal.

$$\tilde{x}(t) = \int_{-\infty}^{\infty} \frac{x(\tau)}{\pi(t-\tau)}\, d\tau \tag{17}$$

Then the amplitude and frequency can be evaluated directly as follows.

$$z(t) = x(t) + i\tilde{x}(t) = A(t)e^{i\theta(t)} \tag{18}$$

$$A(t) = [x^2(t) + \tilde{x}^2(t)]^{1/2}, \quad \theta(t) = \tan^{-1}[\frac{\tilde{x}(t)}{x(t)}] = 2\pi f_o t$$

This transform is frequently evaluated with the help of the FFT [22]. However, the convolution integration via the Fourier spectrum always carries a certain error induced by overlapping or end effect. In order to remove the overlap, both $x(t)$ and $1/t$ of Eq.(17) should be properly fed by the 0s before their Fourier spectrums are evaluated [30]. Because the spectrum of the function $1/t$ (with properly fed 0s) is unavailable now, the calculation is performed on the time domain to remove the end effect.

It was proven in Ref.[23] that, for a data string with a finite range, the Hilbert transform evaluated on the time domain has significantly large error around the two ends of the data string. Moreover, the error deeply penetrates into the interior region. To reduce the penetration effect, the original Hilbert transform is embedded by Gaussian kernel in the form of [23]

$$J[x(t)] = \int_{t_1}^{t_2} \frac{\exp[-(t-\tau)^2/(2\sigma^2)]x(t)}{\pi(t-\tau)\cdot erf(\sqrt{2}\pi f\sigma)} d\tau \tag{19}$$

For a data string of infinite domain, where $t_1 \to -\infty$ and $t_2 \to \infty$, $J[x(t)]$ is approximately equal to the Hilbert transform $\tilde{x}(t)$ with an infinitesimal error whenever $\sqrt{2\pi} f\sigma$ >4. Numerical experiments show that, if the following conditions subject to σ are satisfied, $J[x(t)]$ is almost equal to $\tilde{x}(t)$ and the error penetration distance of the former is much shorter than that of the latter.

$$\sigma > \lambda_{\min}, \ \sigma > 4\lambda_{\max}/\sqrt{2\pi} \tag{20},$$

where $\lambda_{\min}$ and $\lambda_{\max}$ are the shortest and longest wavelength of the sinusoidal function $x(t)$. Whenever the first criterion is violated, for a discrete data string with finite t_1 and t_2, an oscillatory frequency distribution is found around locations where the local wavelength $\approx \lambda_{\min}$. The reason is that the convolution integration should accumulate enough information (from those points where the magnitude of Gaussian kernel function is of order one) to reflect the exact information. In Ref.[23], it is also shown that the error penetration distance of $J[x(t)]$ becomes shorter for a smaller σ. Since the original and modified Hilbert transforms are valid only for a sinusoidal data string, it is easy to extrapolate the data beyond the two ends. Consequently, the error becomes insignificant in the desired data range as will be shown later [23].

III. Results and Discussions

For the sake of completeness, two examples are employed to show the performance of the Fourier spectrum with small error and modified Hilbert transform, respectively. The first example uses the following function.

$$x(t) = 3 + 0.5\bar{t}_i + 2\bar{t}_i^2 + 0.4\sin(100\pi\bar{t}_i) + 0.4e^{-0.2\bar{t}_i^2}\sin(16\pi\bar{t}_i) + 0.2\sin(56\pi\bar{t}_i) + 0.3[1+\bar{t}_i+\bar{t}_i^2]e^{-0.5\bar{t}_i^2}\sin(32\pi\bar{t}_i)$$
$$0 \le t_i \le 10-\Delta t, \ \bar{t}_i = t_i/10, \ \Delta t = 1/400, \ t_i = i\Delta t, \quad i = 0,1,2,...,2047, \tag{21}$$

In order to preserve the periodic condition, the point at $t_{4000} = 10$ (with $x(0) = x(10)$) is dropped. The original data is shown as the upper thin solid line in Fig.2, the non-sinusoidal part is shown as the upper heavy solid line, and the high frequency part is shown as the heavy solid line around horizontal axis. Since the original non-sinusoidal part is generally not known, it is estimated by the iterative filter with $\sigma = 1$ and $m = 30$ (shown as the heavy dashed line). It is found that the estimated and given non-sinusoidal parts are obviously different from each other at the two end. In the interior region, their difference is small as shown. The thin dotted line around the horizontal axis shown in Fig.2 is the estimated high frequency part by dropping corresponding segments of data around the two ends.

If the original data is directly employed to find the spectrum via an FFT program, the resulting spectrum is shown as the long dashed line in Fig.3. In the figure, the exact spectrum (shown as the heavy solid line) is evaluated by the original high frequency part composed of all the sine functions. It uses 4000 uniform spacing points to resolve $\Delta t_{\text{total}} = 10$ together with the odd function mapping. The spectrum evaluated by the original data has a large and exponentially decayed error because of the presence of the non-sinusoidal part and non-periodic condition. The error does contaminate the spectrum of the low frequency part such that the mode of $\sin(16\pi\bar{t}_i)$ is misled. Moreover, even if a mode's frequency can be identified, its amplitude is not known. Consequently, except the frequency

estimation, most spectrums are termed as qualitative outputs. If the estimated high frequency part is employed to find the spectrum, the result contains a much smaller spectrum error than that of the thin dash line and is not shown here due to length limitation. The short dashed line of Fig.3 is the spectrum of the thin dotted line of Fig.2 which drops data around the two ends. Now the error of the estimated spectrum is small with the penalty of shrinking data length. The test case shows that, for a long enough data string, the simple strategy of Ref.[15,16,21] does produce a reasonable spectrum.

The second test case employs the following single sine function to examine the difference between resulting amplitude and frequency estimation via the original and modified Hilbert transforms.

$$y(x) = \sin(\frac{4\pi x}{x_{\text{total}}}), \qquad x_{\text{total}} = 10 \tag{22}$$

In Figs.4 and 5, the estimated amplitudes and frequencies via the original and modified Hilbert transforms are shown, respectively. As compared with the known amplitude and frequency, both methods can not give perfect results around the two ends where $x = 0$ and 10, respectively. The error penetrating distance introduced by the modified Hilbert transform is much shorter than that of the original transform. If the data is extrapolated at the two ends for 600 points, the resulting frequency estimation is shown in Fig.6. Obviously, the error penetration regions at the two ends of the modified version are effectively suppressed to a reasonable level (the maximum error at the two ends is $\pm 0.102\%$ and decays to within $\pm 0.0045\%$ in the region of $1 < x < 9$), while that evaluated by the original Hilbert transform can not achieve the same accuracy.

Finally, the experimental data of Ref.[4-6] is employed to demonstrate the enhanced wavelet transform. Ten set of the u-velocity data were taken from $x = 0.5d$ to $10d$ at the 7 downstream locations along the centerline of the blunt body's wake region as shown in Fig.7, respectively, where $d = 32$mm is the bluff body's width and Re_d =16500 is employed. The free stream turbulence is less than 1%, the non-uniformity of the inflow stream except the boundary layer is within 0.5% error and the blockage ratio of the blunt body in the test section is about 21%. The positive and negative velocities are obtained by employing a dual split-fiber probe (Dantec model 55R55). Those locations in the range of $x = 0.5 - 1.5d$ are within the near wake region, the location of $x = 2d$ is approximately at the end of the near wake region, while that of $x = 3d - 10d$ are at the down stream side of the near wake region. The sampling rate is 500 points per second and the total measuring time interval is 10 seconds. It means that the minimum and maximum frequency resolutions are 0.2 and 250Hz, respectively. Those shown in Table-1 are values of the Hurst exponents corresponding to all the experimental data. All the exponents are in the range from 0.6405 to 0.7229 with small variances that are within the range of $0.5 < H < 1$ and close to 0.5. From the classification of the Hurst analysis, the fluctuation in the flow field is random and belongs to a black noise process. It might repeat itself randomly after some intermediate procedures which first decays and then increases and/or vice versa. Therefore, the wake flow field is a low speed turbulent flow.

The iterative filter was employed to obtain the smooth and high frequency parts which are denoted as u and u', respectively. Figure 8 shows a typical data string's high frequency and smooth parts of point A. The corresponding Fourier spectrum evaluated by the present FFT algorithm is shown in Fig.9. Clearly, if the smooth part is not removed, the spectrum will involve a DC contamination. In order to examine the overall flow properties, mean values of u and u' are calculated, respectively, as

$$\bar{u} = \frac{\Delta t}{U_0 T}\left[\sum_{t=0}^{10\ \text{sec}} u\right], \qquad \bar{u}' = \frac{\Delta t}{U_0 T}\left[\sum_{t=0}^{10\ \text{sec}} (u - u_{\text{low freq.}})^2\right]^{1/2} \tag{23}$$

where $T = 10$ seconds and U_0 = 6m/s is the inlet velocity. The resulting distributions are shown in Fig.10. This figure shows that the near wake region is approximately ended at $x = 2d$ where the mean velocity $\bar{u}$ is obviously recovered from almost zero velocity to a value of $0.62U_0$. Meanwhile, the mean velocity fluctuation $\bar{u}'$ suddenly drops to the level of the downstream wake region.

In order to show the detailed information of the flow field, three typical wavelet coefficient plots corresponding to cases at points A, D, and F of Fig.7, respectively, are discussed. These locations are near the base of the bluff body, at downstream side of the near wake region, and at the far downstream wake region, respectively. If the original Morlet transform is employed, the resulting amplitude plot of point A is shown in Fig.11. The figure shows

that the temporary resolution is very good but the frequency resolution is poor so that the detailed information about mode interaction can not be extracted extensively.

The corresponding wavelet coefficient plot of point A evaluated by the enhanced Morlet transform is shown in Fig.12 with the window parameter $c = 1$. The original data string and plots of estimated amplitude and real parts are involved in the same figure, respectively. It seems that this is the first time that one can look into details of the waveform information of a turbulent data string. For the sake of convenience, a ridge line on the amplitude plot is considered as a waveform. Since this is a first study upon this issue, only the case of c =1 is considered to examine the frequency shift among waveforms. A careful inspection of Fig.12 reveals the followings.

1. At some specific instants of $t =$ constant, there are many waveforms with slightly different wavelengths merged together to form another waveform. There are also waveforms split into several waveforms. These phenomena reflect the energy transform between waveforms whose corresponding frequencies close to each other.
2. Every waveform can not persist indefinitely. It may terminate itself or change the frequency which indicates the energy transform between waveforms.
3. The behavior of the frequency shift is seen for several waveforms. These shifts also reflect the energy changes between waveforms with different and nearby frequencies.
4. Every waveform shown in the wavelet coefficient plot represents a stream with certain velocity fluctuations passing through the region around a measured point. A fluctuation of a waveform may be induced by many finite fluid segments involving a series of small eddies (and hence vortices street in an irregular shape). Moreover, the starting and termination of a waveform reflects the approach and leaving of a specific frequency band's information of a series of eddies, a vortex filament, or a non-uniform and oscillatory flow pocket with variable degree of vorticity, …, etc., with respect to point A. As a consequence, the time-frequency plot shows that the flow structure around the measured point is very complicated and changes rapidly.

Those shown in Figs.13 and 14 are similar plots of that measured at points D and F with c =1, respectively. Many important features are similar to those shown in Fig.12. The main differences are that the waveform of shedding frequency becomes a clear band at the immediate downstream point of the near wake region (see Fig.13) and decays at the down stream location (see Fig.14).

One can extract many information from the wavelet coefficient plot of Fig.12 (and hence Figs.13 and 14). In fact, a waveform with a given window size of c is composed of several Fourier modes of Eq.(6) and is similar to a beat wave whose upper and lower envelopes are reflected by the variation of the amplitude of the waveform. For example, from Fig.12, by tracing the amplitude value along a ridge line, variations of amplitude and frequency are obvious. For the sake of simplicity, several measurements along lines parallel to the time and frequency axes will be separately performed. At first, every $a =$ constant line is employed to approximate a waveform. The distance between two successive amplitude peaks of this approximated waveform is considered as the group or envelope wavelength of the waveform. The mean ratio of the envelope wavelength to $\lambda (= a\pi / 3)$ is estimated by $[30/(\pi a)]$/(no. of peaks) and is a rough measure of the waveform's variation. The corresponding plot of peak numbers and mean ratios are shown in Fig.15. In the high frequency zone, a waveform has a mean envelope wavelength in the order of a few λ s. In the long wave zone corresponding to $\lambda \geq$ 0.035 seconds, a waveform has a mean envelope wavelength longer than 10λ. This means that the main source of the flow randomness comes from the high frequency part which is in the zone including the shedding frequency. In other words, the figure reflects that the high frequency waveforms dominate the energy change of the flow field.

The second measure in the frequency direction is to calculate the approximate waveform number at an instance of time such that one waveform number is counted once a local maximum and minimum pair is found along the vertical direction of Fig.12. The resulting plot is shown in Fig.16. For the sake of convenience, a waveform with $dr/dt < 0$ is referred to as an energy pumping-out waveform while that with $dr/dt \geq 0$ is considered as an energy pumping-in waveform. The figure shows that the number of the energy pumping-in waveforms is approximately equal to that of the energy pumping-out waveforms. Around the two ends where $t \approx 0$ and 10 seconds, the significant number difference between the energy pumping-in and pumping-out waveforms is introduced by the periodic boundary condition of the band-pass limited data string.

Figure 17 shows the estimation of the mean pumping-in and pumping-out energies. The total pumping-in energy is estimated by summing up all r values (with $dr/dt > 0$) between two successive $r_{\min}$s along the vertical direction of a given t. The mean value is then estimated by the ratio of this sum to the pumping-in waveform number. The mean pumping-out energy is estimated in a similar way. In order to exclude the error around $t = 0$ and 10 seconds, the result is shown in the range of $1 < t < 9$ only. Note that, during the range of $3 < t < 4$ seconds, there is an obvious turbulent intermittency of the original data (see Fig.12). Although the corresponding number of the energy pumping-in waveforms before the intermittency is larger than that of the pumping-out waveforms (as shown in Fig.16), the estimated mean pumping-in energy is less than that of the pumping-out (see Fig.17). Nevertheless, both energy measurements decrease up to the point of intermittency. The amplitude plot (an energy measure) of Fig.12 shows that the magnitude of most high frequency waveforms decreases rapidly too. After the intermittency, the mean pumping-in energy rapidly rises and is larger than the mean pumping-out energy. Figure 16 shows that the number difference between the energy pumping-in and pumping-out waveforms reduces during this period. For other cases of point A not shown here, all the intermittencies have a similar tendency. The number difference between the energy pumping-in and pumping-out waveforms around the turbulent intermittency might be due to the time-frequency transform whose detailed mechanism is not known yet.

Starting from an instance on an $a =$ constant line, one might find the nearest $r_{\max}$ in the upward direction and another nearest $r_{\max}$ in the downward direction or vice versa. The normalized bandwidth is defined as the difference of frequencies corresponding to these two $r_{\max}$s divided by $f = 3/(a\pi)$. From these normalized bandwidths along the whole $a =$ constant line, the normalized mean, upper and lower limits of the frequency bandwidth corresponding to the frequency f are estimated and are shown in Fig.18, respectively. The figure shows that the high frequency waveforms with $f > 20$ Hz have a lower limit value of the normalized frequency bandwidth ranged from 10 to 25%. For the long waveforms with $f < 10$ Hz, the value reduces to be less than 5%. It seems that a low frequency waveform frequently shifts its frequency gradually or merges with other waveforms whose frequencies close to it. On the other hand, for the high frequency waveforms, the possibility of the frequency shift and merging between waveforms with frequencies close to each other is relatively low. The mean and upper bandwidth limits reflect these discussions too. Therefore, a high frequency waveform has a larger fraction of the energy transform between waveforms with significant frequency differences than that of a low frequency waveform. This fact can also be verified by the departure between the upper and lower limits which indicates the range of frequency variation of a waveform.

Figure19 shows the real part plot corresponding to that of Fig.12 with a window size parameter value of $c = 2$. A comparison between Figs.12 and 19 reflects the effect of changing the window size upon the wavelet coefficient plot. Since the waveform amplitude shown in Fig.19 is a weighted summation of several waveforms of Fig.12, the resulting waveforms of the former have larger bandwidths than those of the latter. Moreover, the waveform variation in the temporal direction shown in Fig.19 becomes more rapidly than that in Fig.12. Consequently, features of both figures are different from each other to a certain degree. These differences can be explained by comparing Figs.20a and 20b in which the corresponding detailed plots of the high frequency part are shown, respectively. For example, around the point where $(t, a) = (4.5, 0.048)$, Fig.20a shows an in-phase distribution in the vertical direction. On the other hand, around the point (5.8, 0.038), it shows an out-of-phase distribution in the vertical direction. After the weighted summing up procedure which gives Fig.20b, the in-phase region shows an increase of amplitude while the out-of-phase region shows a decrease of amplitude. Similar increase-decrease behaviors of the waveform amplitude can be found in many regions of Figs.20. Consequently, the increase of c improves the temporal resolution but deteriorates the frequency resolution.

Figures 21 through 23 show the number of peaks along $a =$ constant lines, waveform number along $t =$ constant lines, and mean normalized frequency bandwidth of waveforms, respectively, for different window sizes, say $c = 1, 1.5, 2$ and 2.5, etc.. Figure.21 shows that the estimated number of peaks is almost constant with respect to the frequency in the long wave part and linearly increases in the short wave part. The increase of window size increases the number of peaks but is saturated after $c \geq 2$ especially at the low and high frequency side (less than 10Hz and greater than 72 Hz) because of the limitation of sample length and sampling rate, respectively. In Fig.22, the waveform number decreases as c increases, but the waveform number using $c = 2$ closes to that

using $c = 2.5$. The mean normalized bandwidth plot of Fig.23 shows the same tendency of increasing Δf with respect to c as that of Fig.21. These three figures again show the trend that increases the window size c increases the temporary resolution and deteriorates the frequency resolution of the wavelet coefficient plot. Eventually, as c is large enough, the present frequency window effect disappears and the resulting wavelet coefficient plot approaches to that generated by the Morlet transform (see Fig.11). On the other hand, if a very small value of c is employed, the mechanism of capturing the amplitude and frequency variations of a waveform disappears and the resulting wavelet coefficient plot approaches to the corresponding Fourier spectrum of the high frequency data. These two limiting situations are introduced by the well known uncertainty principle of a time-frequency transform [11,12,22].

The above discussions show that different window sizes give different wavelet plots and hence different physical insights. These differences might be corresponding to different length and time scales. It is suspected that: a resulting waveform of using a smaller value of c will properly interact with a solid component with a smaller size or a smaller stiffness while a waveform of using a larger value of c interacts with a larger or a more stiffen component. Since the available experimental data only gives the u velocities at isolated measuring data, it is impossible to give more information from the view point of conservations of the mass, momentum and energy. Nevertheless, the present study indicates the necessity of organizing proper experiments to look into details of a turbulent flow field.

Equations (13) and (16) show that, along a single $a =$ constant line, the integration procedure of the wavelet plot accumulates information over a region on the time-frequency plane. The integration introduces a re-arrangement of the original data string that deteriorates both the spectral and temporary resolutions. In order to precisely look into the temporal behavior of a single waveform, the modified Hilbert transform is employed. For the sake of convenience, a rectangular band-pass limited filter is employed to define a waveform. For example, a waveform involving the 72 Hz mode (the shedding frequency mode) using a 0.3Hz bandwidth completely excludes all the Fourier modes outside the range of 71.7 to 72.3Hz and preserves all modes within it. This waveform is referred to as the 72Hz waveform or the shedding frequency waveform. After carefully checking all the wavelet coefficient plots, the bandwidths of 0.3, 0.6 and 1.0Hz are chosen to reflect consistent information for all cases. Those shown in Fig.24 are the 72Hz waveform data, amplitude, and frequency of a case of point A, respectively. For the sake of clarity, the vertical scales of data and amplitude plots are shifted upward by a value of 0.1 for different frequency bandwidths as shown and that of the frequency plot is shifted by a value of 10Hz, respectively. These figures show that a waveform with a wider bandwidth gives a more complicated structure. The amplitude's magnitude reflects the envelope of the data string exactly. The original frequency plot exhibits an oscillatory behavior over a finite bandwidth of 4Hz which is introduced by the insufficient sampling rate such that only about 7 points are employed to resolve a wave length. The frequency plot of Fig.24 has been smoothed by the iterative filter using $\sigma = 0.1, m = 10$. The sharp kinks (for example, at $t = 1.5$ seconds of the 0.3Hz case) are induced by the almost vanishing amplitude. Those shown in Fig.25 are results of the 36 Hz waveform which involve the first sub-harmonic mode. Although it can not be clearly seen from these figures, the corresponding mean amplitude of this figure is larger than that of the 72Hz. It reflects that, within the near wake region, the first sub-harmonic mode dominates the flow fluctuation because the shedding vortices can not be directly rolled into the base region of the bluff body. This result consists with the extensive studies of Ref.[9] that the low frequency modulation dominates this zone.

In the turbulent flow studies, it is interesting to examine quantitatively the energy and energy variation corresponding to the shedding frequency mode and sub-harmonic modes. The energy variation is related to the energy cascade between modes with different frequencies. However, this idea is an average over the sample time and whole flow field that cannot provide time varying information. Instead of searching the energy cascade between Fourier modes, the energy cascade between waveforms at isolated point is a practical and available approach. Since the employed experimental data are measured at isolated points and provided the horizontal velocity component only, it is impossible to obtain the true magnitude of energy and energy variation here. Fortunately, the present study can provide a fraction of physical insight from these limited data.

Those shown in Fig.26a-c are measures of the mean energy of different waveforms (estimated by the summation of the local amplitude's squares, say $\sum r^2(t)$, corresponding to a waveform) with respect to the

x locations for different spectrum band-widths of $0.3, 0.6,$ and 1Hz, respectively. These data are calculated from all the 10 experiments and at all measuring points. The lengths of vertical bars are the estimated sample deviations. Note that the difference between the maximum and minimum values is about 2.5 times longer than the estimated deviation that reflects the random nature of the turbulent flow. All the estimated sample deviations in the near wake region are much larger than those in the downstream wake region. This fact also proves that both the random nature and low frequency modulation in the near wake region are much more serious than those in the downstream wake region as concluded in Ref.[8-10].

For all the window sizes, the estimated mean energy measure of the first sub-harmonic waveform is almost the largest one among all the waveforms in the whole wake region as noted previously. In the near wake region, the mean energy of the first sub-harmonic waveform is much larger than all the other waveforms. It means that the first sub-harmonic waveform rapidly receives energy from the shedding frequency waveform and release energy to the second and third sub-harmonic waveforms in the near wake region. At point D, which is at the end of the near wake region, two main streams passing through the bluff body's two sides merge together. The energies of the shedding frequency waveform and main stream dominate the total energy here so that the first sub-harmonic waveform's energy drops to the third one. In the downstream wake region, the energy of this sub-harmonic waveform gradually transfers energy to other sub-harmonic waveforms and damps out simultaneously.

Within the near wake region where $x \le d$, the energy of the shedding frequency waveform is again the smallest one because the main stream can not frequently reach here. It is interesting that the sub-harmonic waveforms of the 9 and 18 Hz also show a trend of decay from $x = 0.5d$ to $x = d$. At the further downstream location, the 18 Hz waveform decays in an oscillatory manner while the 9 Hz waveform gains energy up to $x = 1.5d$ and then decays, too.

At the far downstream location, say at region where $x \ge 5d$, energies of all the sub-harmonic waveforms are competitive with that of the shedding frequency waveform. Up to the location where $x = 10d$, because all the high frequency waveforms (whose $f \ge 72$ Hz) decay to a very small energy level, these sub-harmonic waveforms dominate the flow field that quantitatively verifies the conclusion of Ref.[9].

Since the difference of maximum and minimum values of the estimated energy measures is larger than the estimated deviation shown in Fig.26, the above discussions are restricted to the mean energy measure only. In fact, an unpredictable variation of the energy measures always exists.

Those shown in Fig.27a-c are the estimated energy changing rates corresponding to those of Fig.26, respectively. The measure of energy changing rate is estimated by the summation of $|r^2(t+\Delta t) - r^2(t)|$ over the whole sampling period. These energy changing rates are indices of the energy pumping in and out of waveforms. These figures show that the main source of the energy recover is provided by the shedding frequency waveform. Again, the vertical bars denote the estimated sample deviation among 10 experimental data. The corresponding ranges between the maximum and minimum values are also about 2.5 times wider than the estimated sample deviation. Measures and deviations of energy changing rate of all the sub-harmonic waveforms are much smaller than that of the shedding frequency waveform because these waveforms gradually receive energy from the high frequency waveforms and transfer energy to the mean flow. Among three sub-harmonic waveforms, the 18Hz waveform is the greatest one at $x = 0.5d$ for all the frequency bandwidths. At other locations in the near wake region, there is no rule to describe the measure of energy changing rate. In the downstream wake region, among all the sub-harmonic waveforms, the 36 Hz waveform has almost the greatest mean energy changing rate as shown. The large deviation value of the shedding frequency waveform in the near and downstream wake regions again reflects the random nature of the flow field. Therefore, it seems that one cannot obtain a definite rule of the tendency of the measure of the energy changing rate.

The complexity of the flow field can also be reflected by comparing the properties between wide bandwidth waveforms. In Fig.28, measures of the average energy of waveforms in the ranges of 4.5-13.5Hz, 13.5-27Hz, 27-54Hz, and 54-108Hz are shown, respectively. The main features are similar to those shown in Fig.26 of narrow bandwidth waveforms except some discrepancies. Now the shedding frequency waveform (with the widest bandwidth of 54Hz) has an energy measure larger than that of both the 9 and 18Hz waveforms in the near wake

region and competes with that of the first sub-harmonic waveform. Moreover, the tendency of monotonous decays in the region where $x > 1.5d$ shows that the shedding frequency waveform's energy is released to the sub-harmonic waveforms (eventually recovers to the mean velocity) and damped out simultaneously.

As to the estimation of energy changing rate, magnitudes of these wide band-width waveforms show a regular sequence (see Fig.29). Obviously, a waveform with a shorter wavelength has a larger energy changing rate than those with longer wavelengths. It seems that a long wavelength waveform has a small energy transfer rate because the corresponding velocity gradient is small. In other words, both energy transformations of recovering to the uniform flow velocity and being damped out are very slow. On the other hand, a short wave waveform has a large velocity variation in spatial direction and is easy to induce flow instability so as to pumping energy out of it through viscosity dissipation. The total energy pumping rate from the high frequency waveform to the low frequency waveforms is also very small because its order of magnitude should be equal to that of the low energy changing rate of the sub-harmonic waveforms. These discussions quantitatively verify the well known fact that, in the downstream location after the near wake region, all the waveforms inefficiently and gradually pump energy back into the low frequency waveforms and eventually cause the mean velocity recovering to the original U_0 as shown in Fig.10.

The above discussions of employing the modified Hilbert transform certainly indicate two valuable rewards:

1. Measures of the energy and energy exchanging rate of a waveform can be precisely extracted. With these data, models of energy cascade between waveforms can be constructed in future.
2. The resulting variations of data, amplitude, frequency, energy, and energy changing rate of waveforms with different frequency bandwidths can be employed to explain the existing detailed mechanisms.

So far it is not known how to employ a suitable bandwidth of the waveform for both wavelet calculation and waveform evaluation via the modified Hilbert transform. However, the use of several bandwidths, the wavelet coefficient plot, measures of both the energy and energy changing rate of different waveforms gives many detailed information which can clearly explain many known phenomena. The authors believe that, using the same procedure of this study, one can monitor many detailed effects of a flow control mechanism upon a turbulent flow field or examines details of a turbulent flow field without difficulty.

IV. Conclusion

The enhanced continuous wavelet transform, modified Hilbert transform and an FFT algorithm with small error are employed to examine the $u-$ velocity data of a low speed flow over a bluff body. The flow field is proven to be turbulent via the Hurst analysis. Many qualitative details are reflected by the resulting wavelet coefficient plots which are not seen before. By using the modified Hilbert transform, the amplitude and frequency of a waveform can be precisely evaluated. The quantitative measures of energy and the total energy exchanging rate of a waveform can then be explicitly calculated. With this new tool in hand, the related further works will be addressed on: (1) how to relate the window size of the band-pass limited spectrum to physics so that it can be reasonably defined; (2) to develop new methods to extract unknown information from the two-dimension wavelet coefficient plot; and (3) to develop models to reflect the mechanism of energy cascade among different waveforms.

Acknowledgments

This work is supported by the National Science Council of Taiwan under the grant number NSC-93 -2212-E006-037. The authors are also grateful to professor Miau of National Cheng Kung University and Prof. Wang of Gau-Yuan Institute of Technology, Taiwan for their kindness of suggesting the experimental data.

References

[1]Bloor, M. S., "The Transition to Turbulence in the Wake of a Circular Cylinder," *J. Fluid Mech.*, Vol.19, pp.290-303, 1964.

[2]Miau, J. J., Yang, C. C., Chou, J. H., and Lee, K. R., "Suppression of Low-Frequency Variations in Vortex Shedding by a Splitter Plate Behind a Bluff Body," *J. Fluids and Structures*, Vol.7, pp.897-912, 1993.

[3]Miau, J. J., Yang, C. C., Chou, J. H., and Lee, K. R., "A T-shaped Vortex Shedder for a Vortex Flowmeter," *Flow Measurement and Instruments 4*, No. 4, pp.259-267, 1993.

[4]Miau, J. J., Wang, J. T., Chou, J. H., and Wei, C. Y., "Characteristics of Low-Frequency Variations Embedded in Vortex Shedding Process," *J. Fluids and Structures*, Vol.13, pp.339-359, 1999.

[5]Miau, J. J., J. T. Wang, J. H. Chou and C. Y. Wei., "Low-Frequency Fluctuations in the Near-Wake Region of a Trapezoidal Cylinder with Low Aspect Ratio," *Journal of Fluids and Structures* Vol.17/5，pp.701-715, 2003.

[6]Wang, C. T., "Investigation of Low-Frequency Variations Embedded in Vortex Shedding Process," *Ph.D dissertation*, Department of Aeronautics and Astronautics, National Cheng-Kung University, June 2000.

[7]Hu, C. C., Miau, J. J., and Chau, J. H., "Instantaneous Vortex-Shedding Behavior in Periodically Varying Flow," *Proc. R. Soc. Lond. A*, Vol. 458, pp. 911-932, 2002.

[8]Wu, S. J., "Instantaneous Properties of Low-Frequency Modulations and Three-Dimensionality Associated with Vortex Shedding," *Ph. D. Dissertation*, National Cheng Kung University, June 2003.

[9]Miau,J. J., S. J. Wu, C. C. Hu, and J. H. Chou, "Low Frequency Modulations Associated with Vortex Shedding form Flow over Bluff Body," *AIAA J*., vol.42, no.7, pp.1388-1397, 2004.

[10]Wu, S. J., J. J. Miau, C. C. Hu, and J. H. Chou, "On Low-Frequency Modulations an Three-Dimensionality in Vortex Shedding behind Flat Plates," *J. Fluid Mechanics*, vol.526, pp.117-146, 2005.

[11]Grossman, A. and Morlet, J., "Decomposition of Hardy Functions into Square Integrable Wavelets of Constant Shape," *SIAM J. Math. Anal.*, Vol. 15, No. 4, pp. 723-736, 1984.

[12]Farge, M., "Wavelet Transforms and Their Applications to Turbulence," *Annu. Rev. Fluid Mech*., Vol. 24, pp. 395-457, 1992.

[13]Huang, N. E., Z. Shen, and S. R. Long, "A New View of Nonlinear Water Waves: the Hilbert Spectrum," *Annual Reviews of Fluid Mechanics*, vol.51, pp.417-457, 1999.

[14]Huang, N. E., Shen, Z., Long, S. R., Wu, M. C., Shih, H. H., Zheng, Q., Yen, N. C., Tung, C. C. and Liu, H. H., "The Empirical Mode Decomposition and the Hilbert Spectrum for Nonlinear and Non-stationary Time Series Analysis," *Proc. R. Soc. Lond. A*., vol. 454, pp.903-995, 1998.

[15]Jeng, Y. N., C.T. Chen, and Y. C. Cheng, "A New and Effective Tool to Look into Details of a Turbulent Data String," *Proceedings of 12th National Computational Fluid Dynamics Conference*, Kaohsiung, paper no. CFD12-2501, Aug. 2005.

[16]Jeng, Y. N., and Cheng, Y. C., "The New Spectrogram Evaluated by Enhanced Continuous Wavelet and Short Time Fourier Transforms via Windowing Spectrums," *Proceedings of 18th IPPR conference on Computer Vision, Graphics and Image Processing (CVGIP2005), Taipei R.O.C.*, pp.378-383, Aug. 2005.

[17]Jeng, Y. N., Huang, P. G., and Chen, H., "Wave Decomposition in Physical Space Using Iterative Moving Least Squares Methods," *Proceedings of 11-th National Computational Fluid Dynamics Conference, Tai-Tung R.O.C.*, paper no. CFD11-0107, Aug. 2004.

[18]Jeng, Y. N., Cheng, Y. C., and Yang, T. M., "Wave Decomposition Across Discontinuity Using Iterative Moving Least Squares Methods," *Proceedings of 11-th National Computational Fluid Dynamics Conference, Tai-Tung R.O.C.*, paper no. CFD11-0110, Aug. 2004.

[19]Jeng, Y. N. and P. G.. Huang, "Evaluation of Derivatives from Composite Wave via Iterative Filter and A Numerical Method of Solving Partial Differential Equations," *Proceedings of 11-th National Computational Fluid Dynamics Conference, Tai-Tung, Taiwan*, paper no. CFD11-0111, Aug. 2004.

[20]Jeng, Y. N., Huang, P. G.. and Chen, H., "Filtering and Decomposition of Waveform in Physical Space Using Iterative Moving Least Squares Methods," *AIAA paper* no.2005-1303, Reno Jan. 2005.

[21]Jeng, Y. N. and Cheng, Y. C., "A Simple Strategy to Evaluate the Frequency Spectrum of a Time Series Data with Non-Uniform Intervals," *Transactions of the Aeronautical and Astronautical Society of the Republic of China*, vol.36, no.3, pp.207-214, 2004

[22]Bendat, J. S, and Piersol, A. G., *Random Data Analysis and Measurement Procedures*, 3rd ed., John Wiley & Sons, New York, Chapters 10 & 11, pp.349-456, 2000.

[23]Jeng, Y. N., "Modified Hilbert Transform for Non-Stationary Data of Finite Range," *7th National CFD Conference, Taiwan*, pp.15-22, Aug. 2000.

[24]Richardson, L.F., *Weather prediction by numerical process*, Cambridge Univ. Press, 1922.

[25]Kolmogorov, A. N., "The local structure of turbulence in incompressible viscous fluid for very large Reynolds number", *Dokl. Akad. Nauk SSSR* 30, 9, 1941 (Reprinted in Proc. Royal Soc. London A 434, 913; 1991).

[26]Hurst, H.E., "Long-Term storage in reservoirs", *Trans. Am. Soc. Civ. Eng.*116, 770, 1965.

[27]Lamperti, J.W., "Semi-Stable Processes", *Trans. Am. Math. Soc*.104, pp.62-74, 1962.

[28]Mandelbrot, B. B., *Gaussian Self-Affinity and Fractals*, Springer; NewYork, 2002.

[29]Huynh, H. T, "Accurate Monotone Cubic Interpolation," *SIAM J. Number. Anal*. vol.30, no.1, pp57-100, Feb.1993.

[30]Brigham, E. O., *The Fast Fourier Transform*, Prentice-Hall Inc., Englewood Cliffs, New Jersey, 1974.

Table 5.1
Average Hurst exponent H and Variance σ of H

	P_b	A	B	C	D	E	F	G
H	0.6882	0.6908	0.708	0.7229	0.7017	0.6405	0.6829	0.6978
σ	0.0233	0.0415	0.0801	0.0121	0.0335	0.0199	0.0188	0.0201

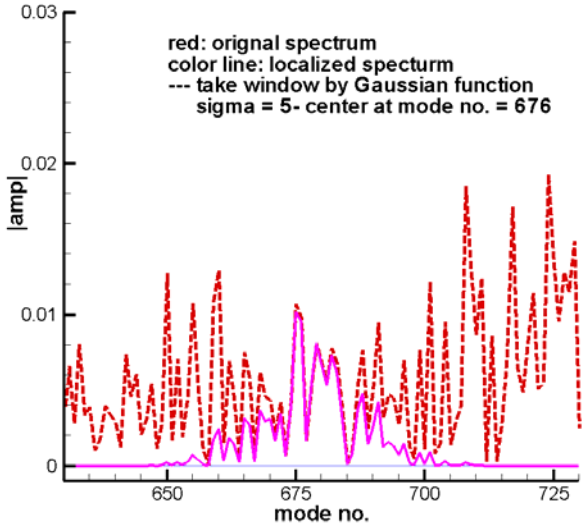

Fig.1 The original and band-pass limited spectrums: the dashed line is the original spectrum and the solid line is a band-pass limited spectrum.

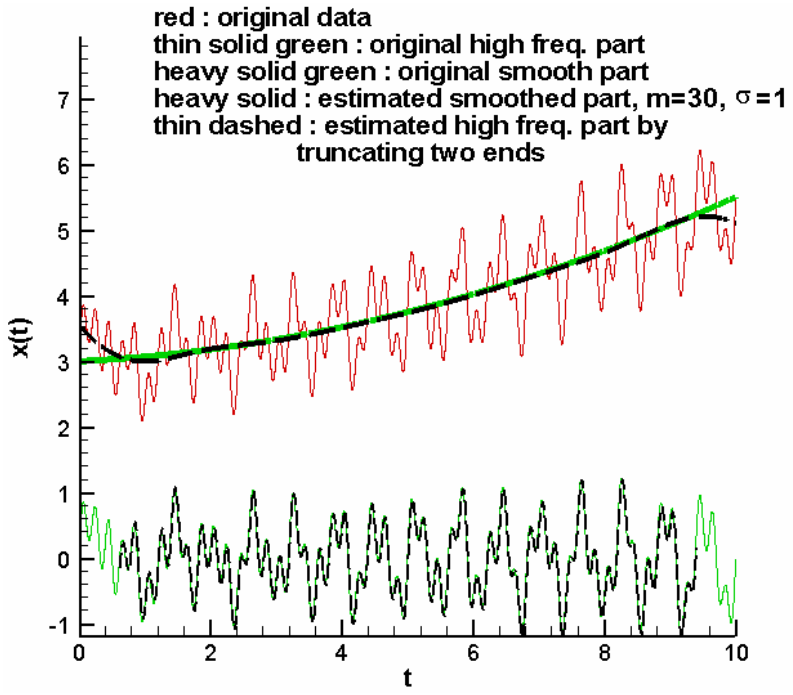

Fig.2 The original data, original and estimated non-sinusoidal plus low frequency parts are shown as the thin solid red, heavy green, and dashed black lines around $x(t) = 3$, respectively. The original and estimated high frequency parts are shown as the thin green solid and black dashed lines around $x(t) = 0$, respectively.

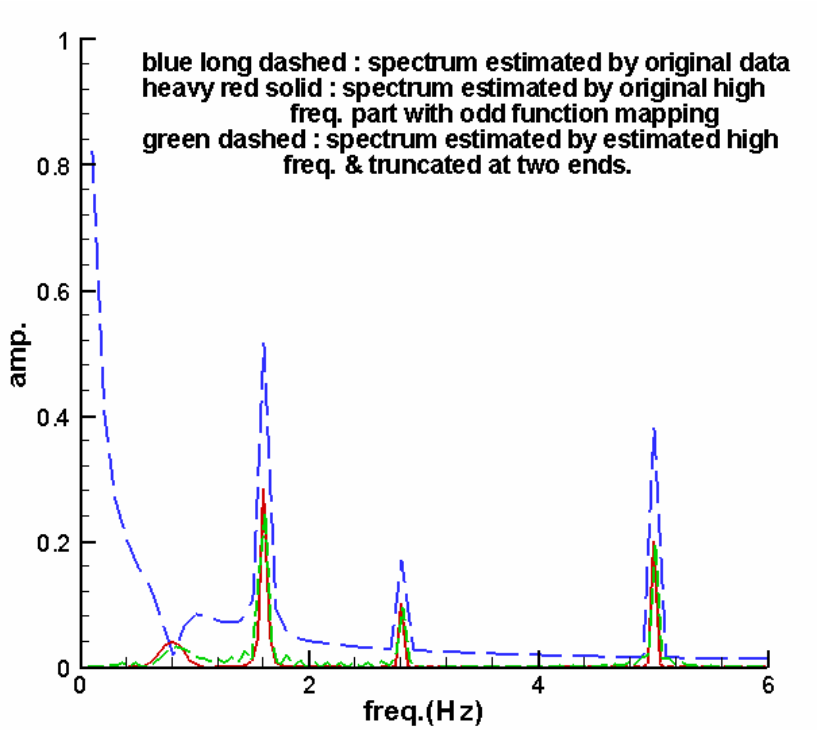

Fig.3 The spectrum of the original data of Eq.(20) is shown as the long dashed line. The exact spectrum is shown as the red solid line and the spectrum of the estimated high frequency is shown as the green dashed line, respectively.

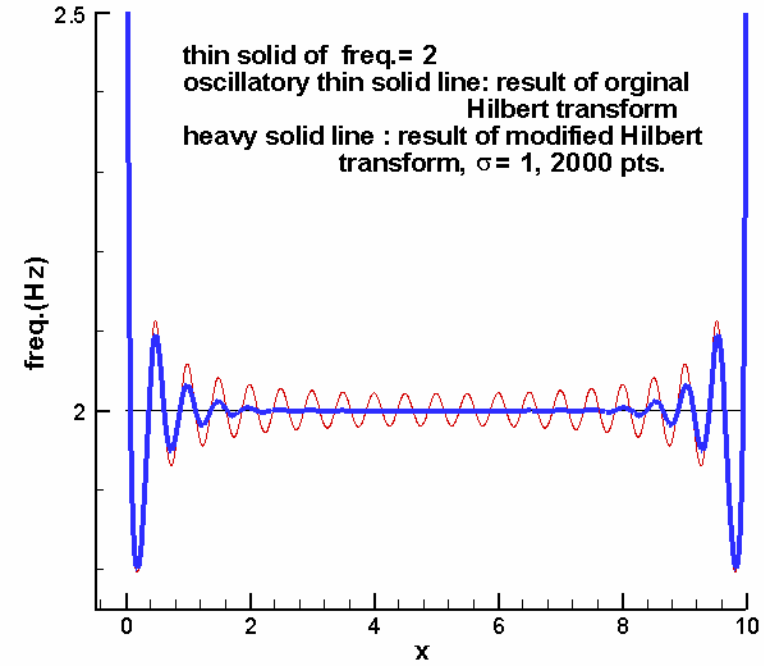

Fig.4 Comparison between the exact frequency ($f = 2$ Hz) and those estimated by the original (thin solid line) and modified (heavy solid line) Hilbert transform.

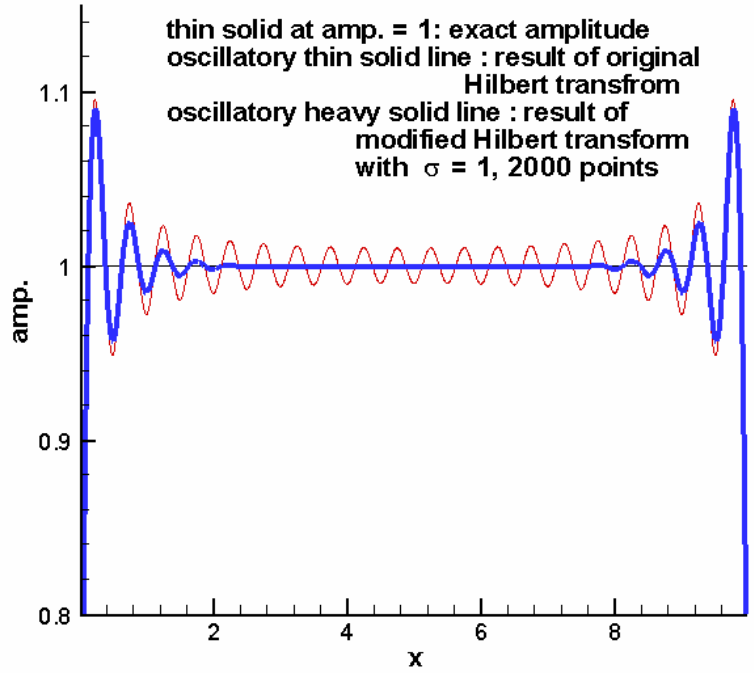

Fig.5 Comparison between the given amplitude (=1) and those estimated by the original (thin solid line) and modified (heavy solid line) Hilbert transform.

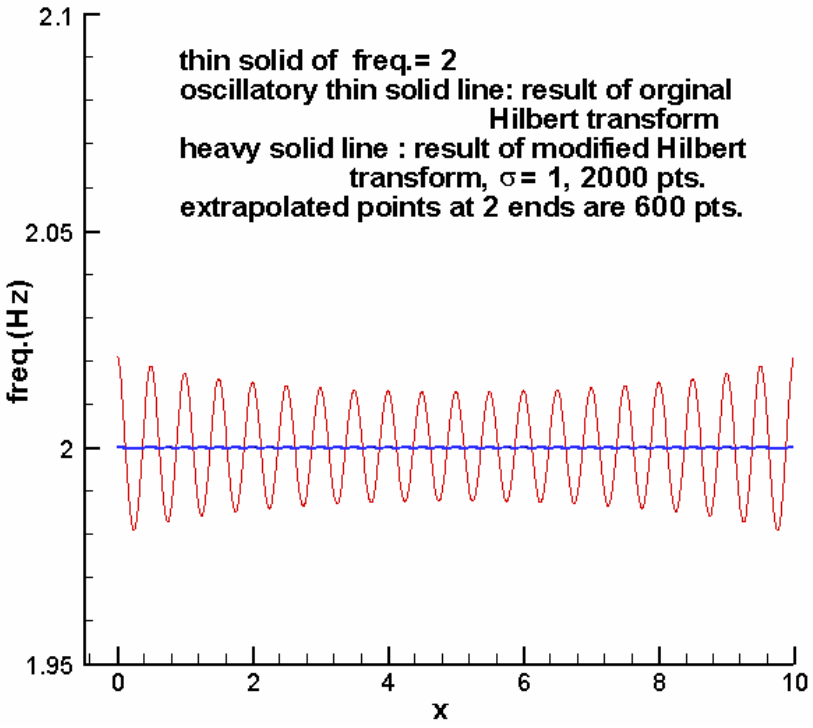

Fig.6 Comparison between the given frequency (=2) and those estimated by the original (thin solid line) and modified (heavy solid line) Hilbert transform; the data are extended to $x = -3$ and $x = 13$.

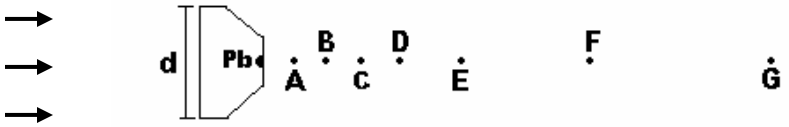

Fig.7 A schematic drawing of wake flow and setup of measuring position, d = 32 mm. The locations are: 0.5d for A, 1d for B, 1.5d for C, 2d for D, 3d for E, 5d for F, and 10d for G.

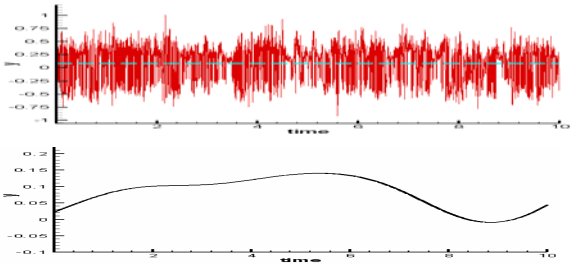

Fig.8 The high frequency and smooth parts of a case measured at point A.

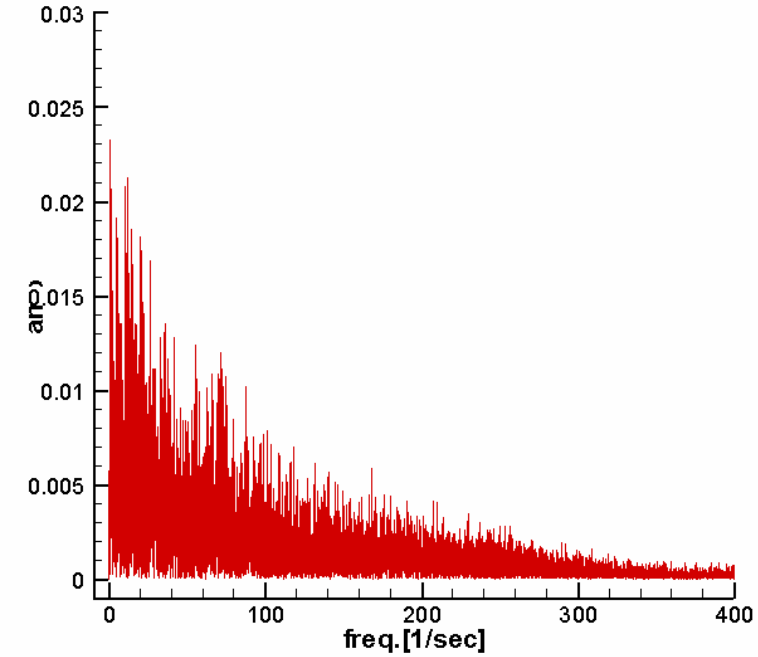

Fig.9 The spectrum of the high frequency part of Fig.8.

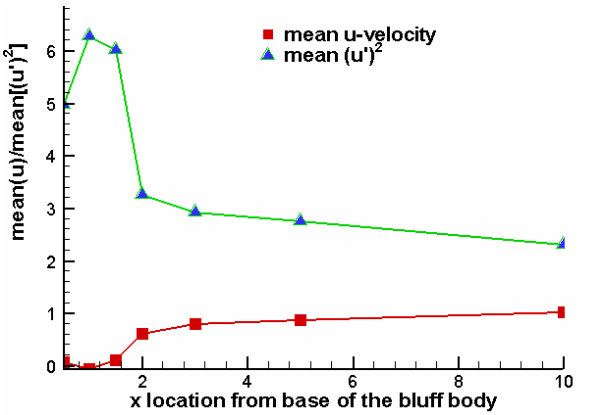

Fig.10 The mean u/U_0 and u'/U_0 velocities measured at different locations.

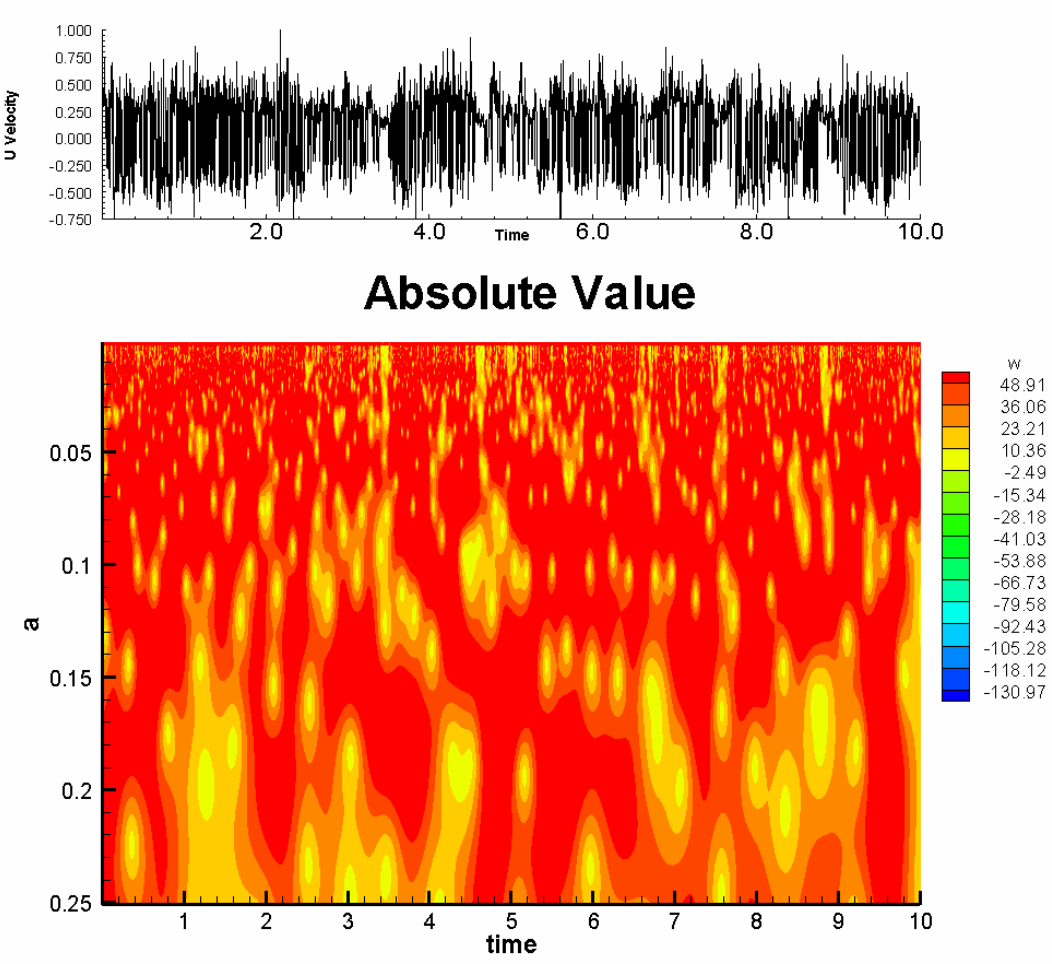

Fig.11 The original data of a case measured at point A and the amplitude plot of the wavelet coefficient evaluated by the original Morlet transform.

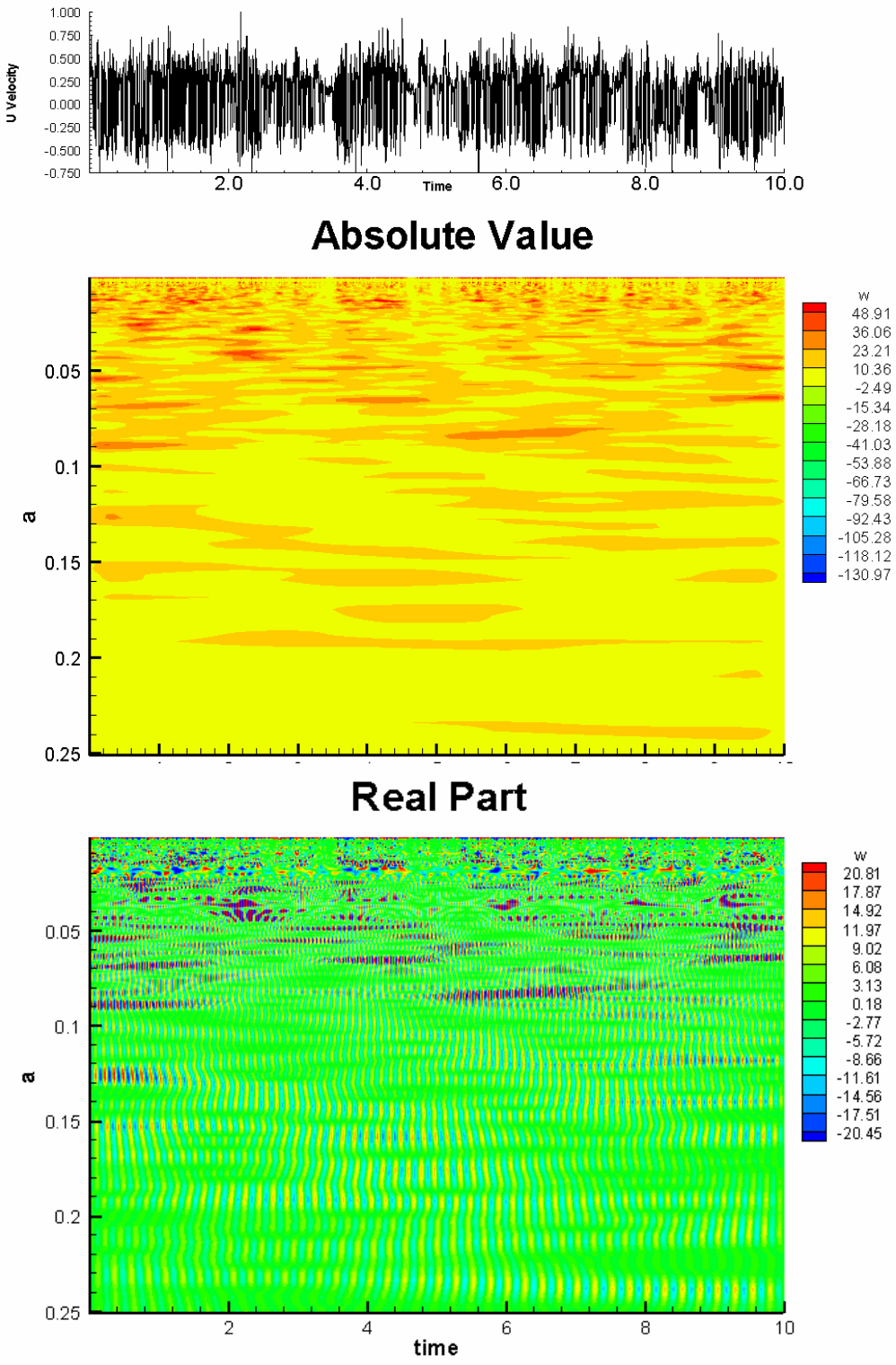

Fig.12 The amplitude and real part of the wavelet coefficient plot of case A, generated by the enhanced Morlet transform with $c = 1$.

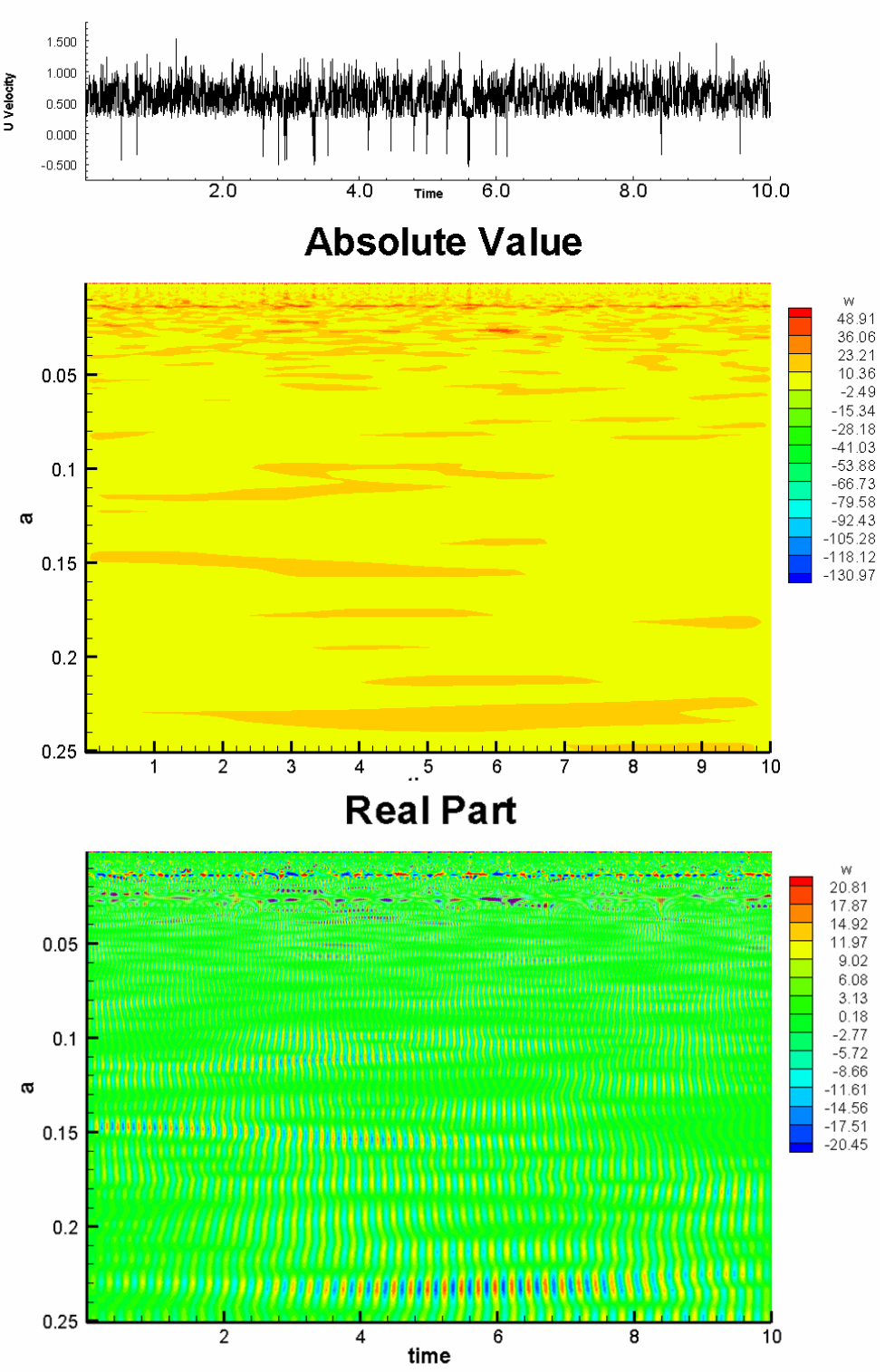

Fig.13 The amplitude and real part of the wavelet coefficient plot of case D, generated by the enhanced Morlet transform with $c = 1$.

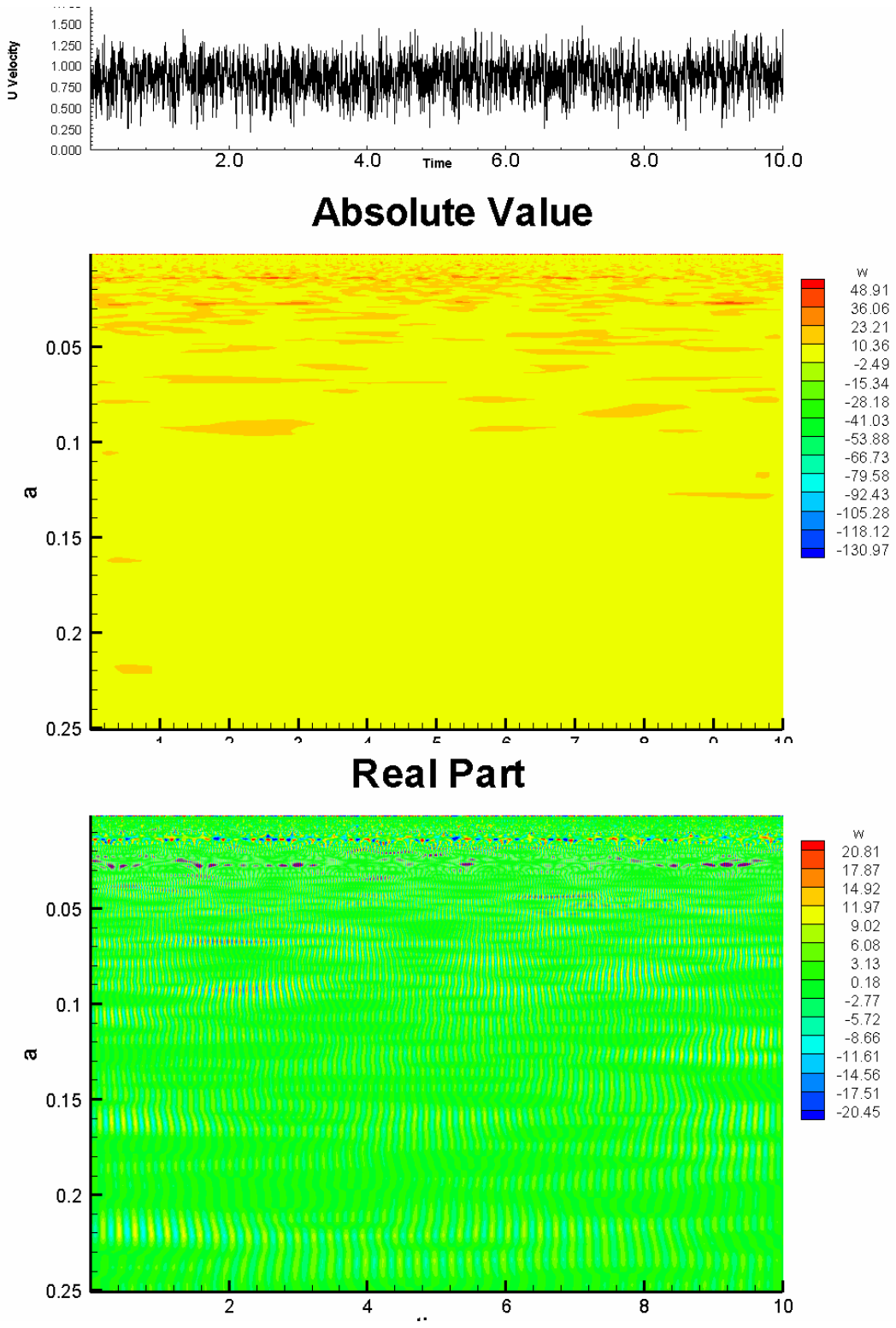

Fig.14 The amplitude and real part of the wavelet coefficient plot of case F, generated by the enhanced Morlet transform with $c = 1$.

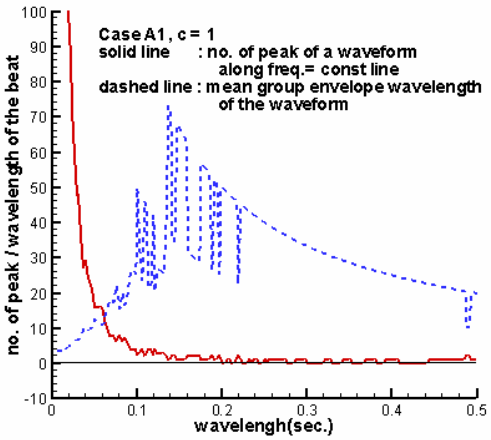

Fig.15 The estimated number of peaks and envelope wavelength of a waveform at different frequency.

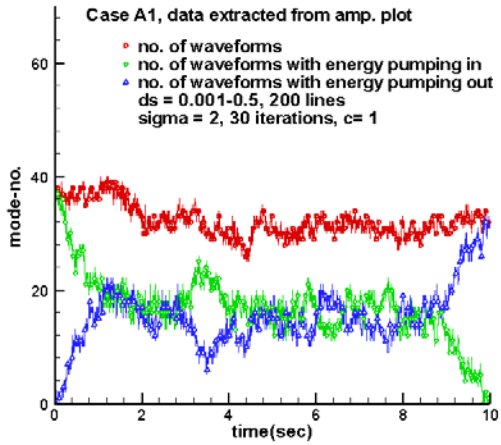

Fig.16 The estimated waveform number at different instance of time: the square symbol line represents the overall waveform number; the circular symbol line represents waveform with energy pumping-in; while the triangle symbol line represents waveform with energy pumping-out.

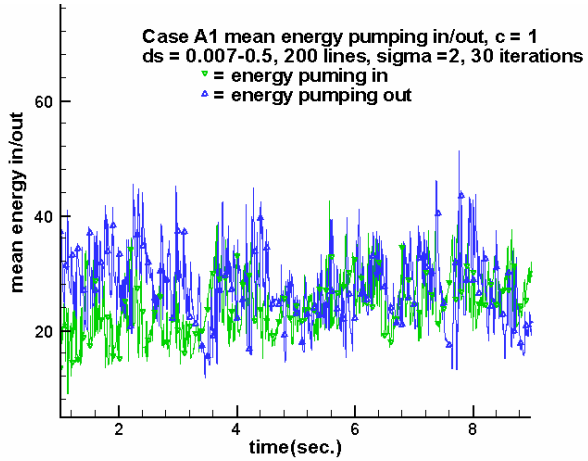

Fig.17 The averaged energy measures of pumping in and out from waveforms at difference instance: the gradient symbol line represents pumping-in energy and the triangle symbol line represents pumping-out energy.

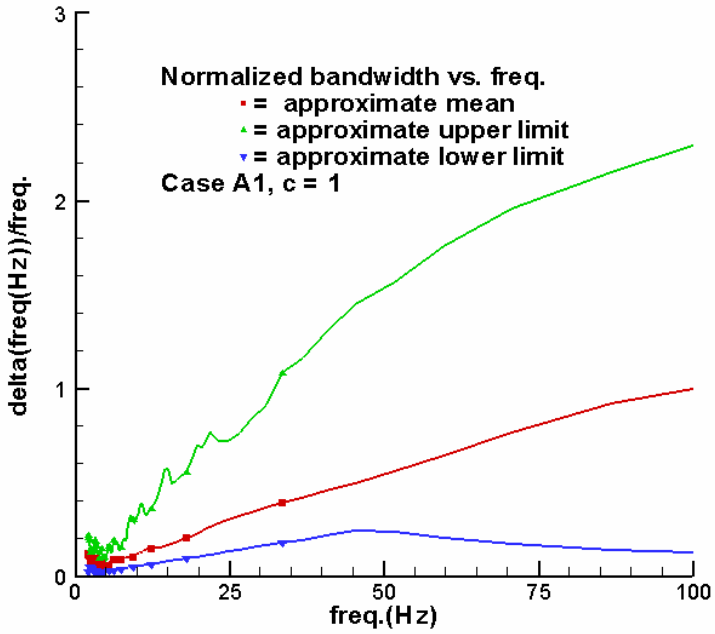

Fig.18 The estimated mean, upper and lower bounds of the normalized bandwidth of each waveform.

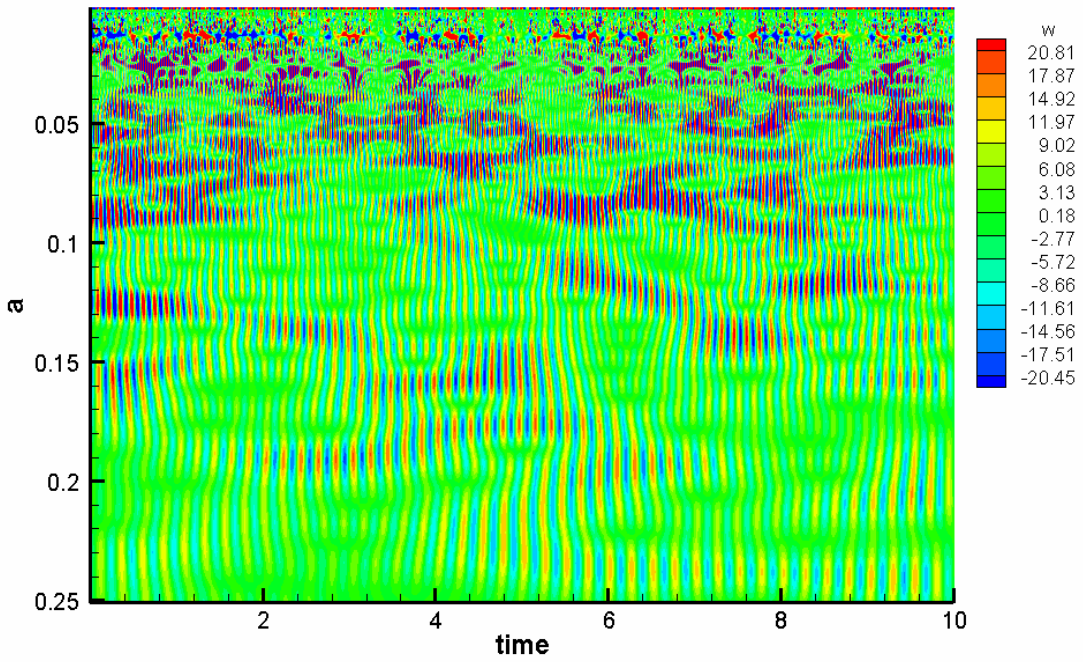

Fig.19 The real part of an case measured at point A, generated by the proposed modified Morlet transform with $c = 2$**.**

(20a)

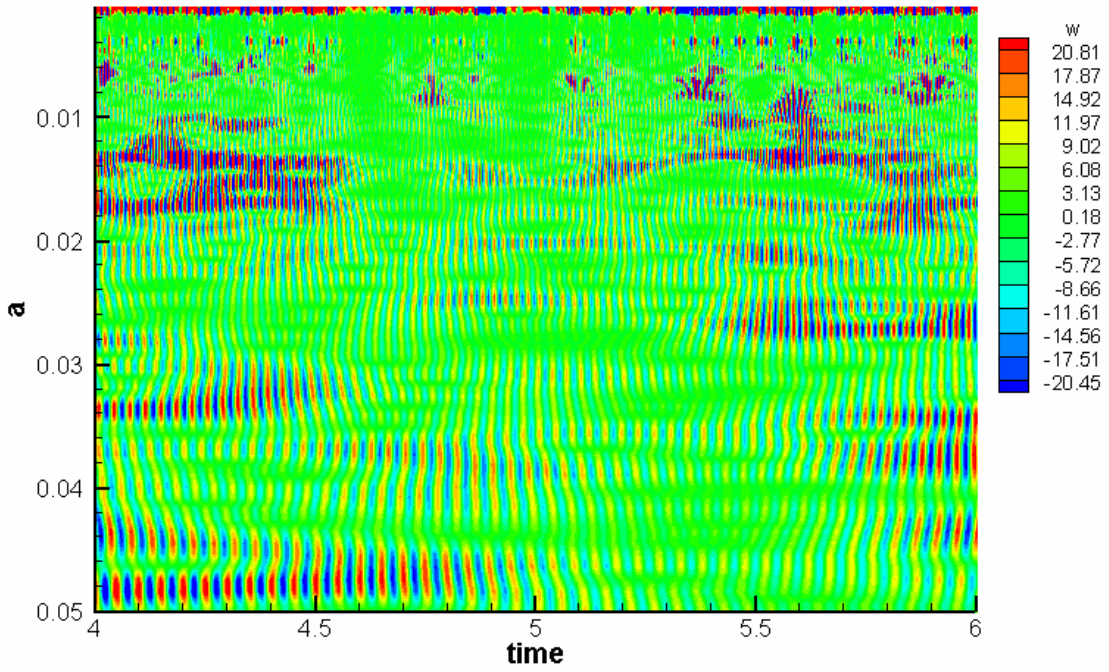

(20b)

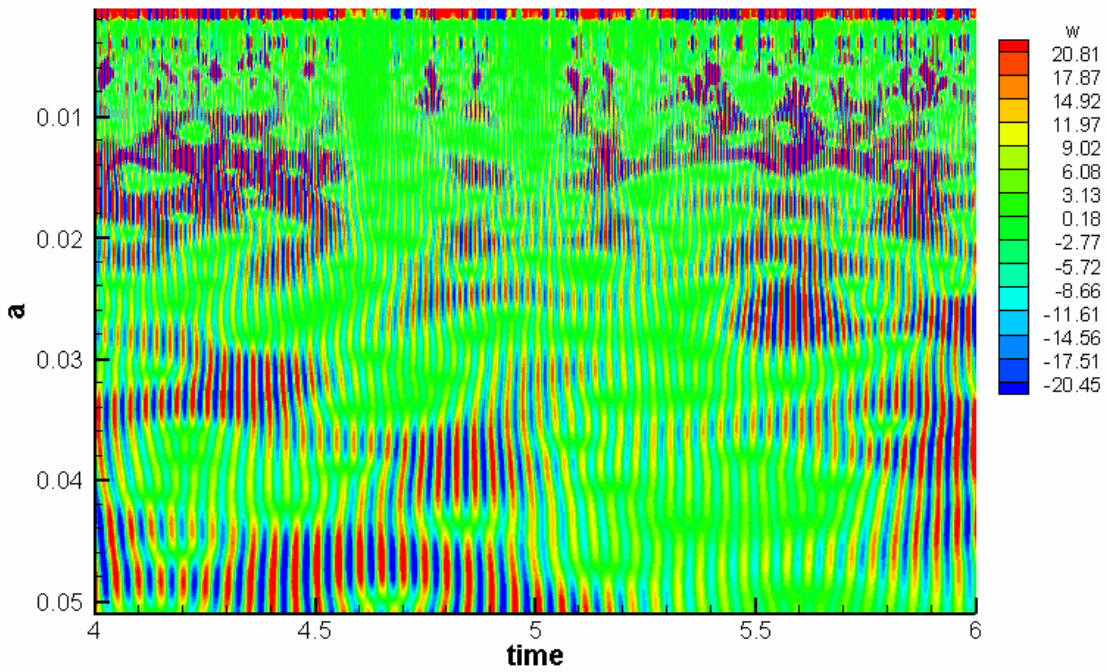

Fig.20 Comparison of high frequency part of real part plots: (a) uses $c = 1$ (corresponding to Fig.12) and (b) uses $c = 2$ (corresponding to Fig.19).

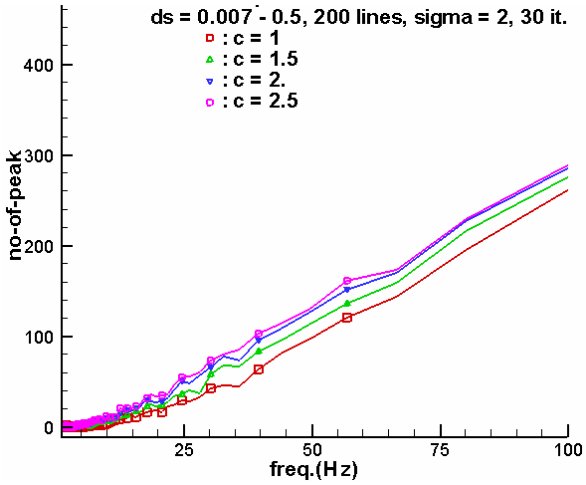

Fig.21 The estimated number of peaks along a = constant line for different window sizes.

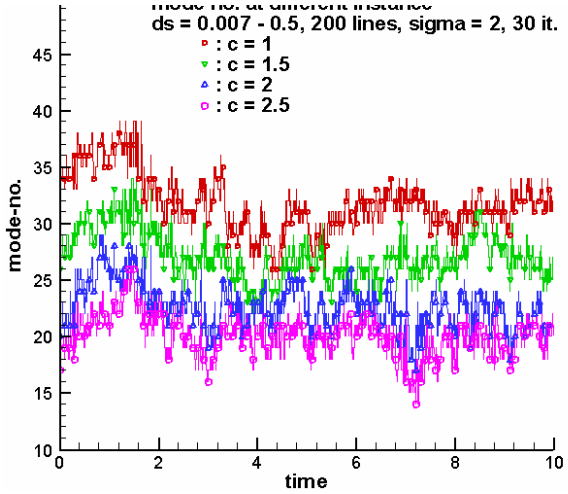

Fig.22 The estimated waveform number at different instance for different window sizes.

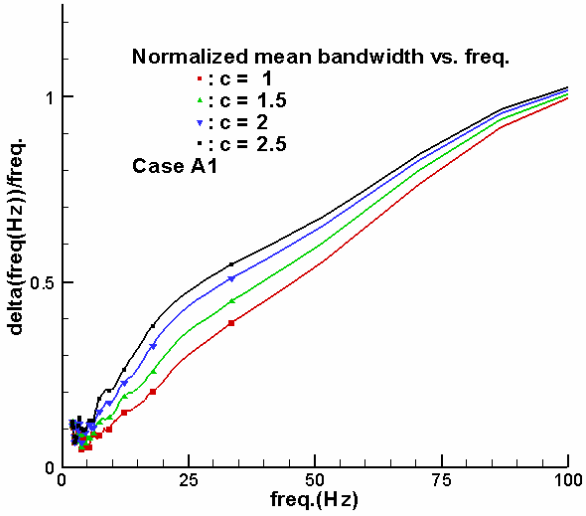

Fig.23 Comparison of the mean frequency bandwidths of waveforms using different window sizes.

(24a) **(24b)**

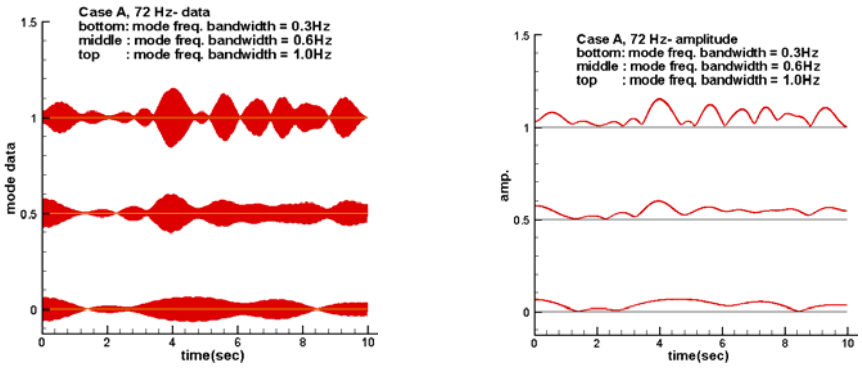

(24c)

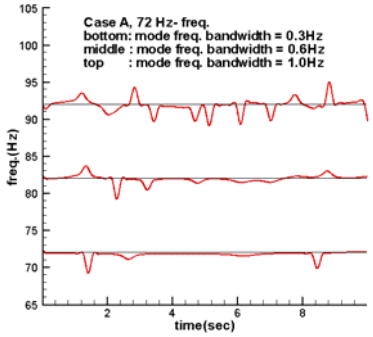

Fig.24 The 72Hz rectangular waveform data of the Case A with different bandwidth: (a) is data; (b) is amplitude; and (c) is frequency. Three bandwidths of 0.3, 1.2 and 1.5 Hz, are employed.

(25a) **(25b)**

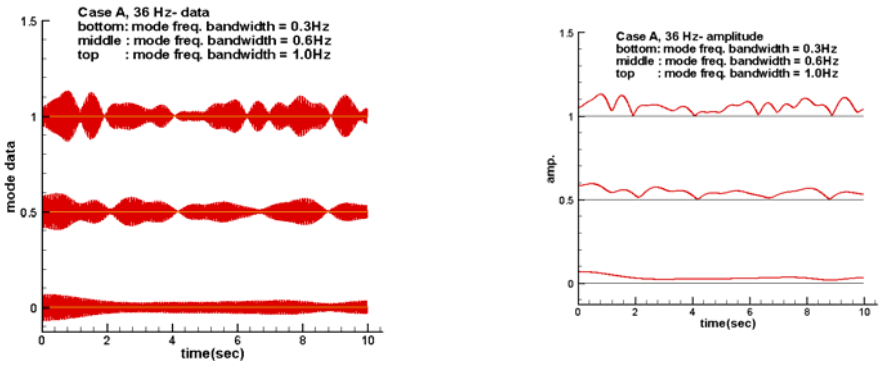

(25c)

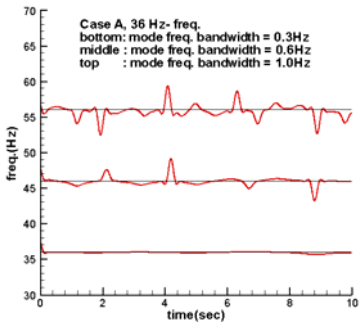

Fig.25 The 36Hz rectangular waveform data of the Case A with different bandwidth: (a) is data; (b) is amplitude; and (c) is frequency. Three bandwidths of 0.3, 1.2 and 1.5 Hz, are employed.

(26a)

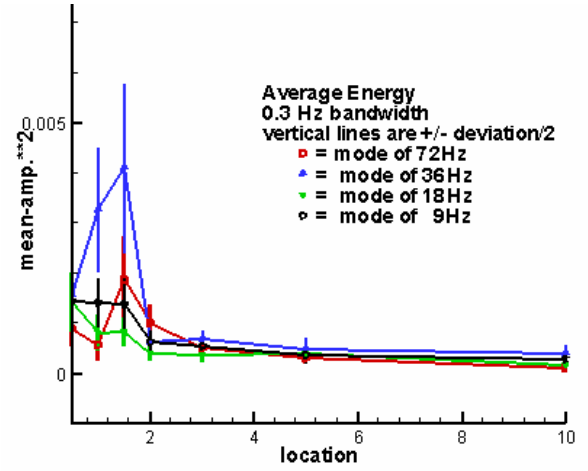

(26b)

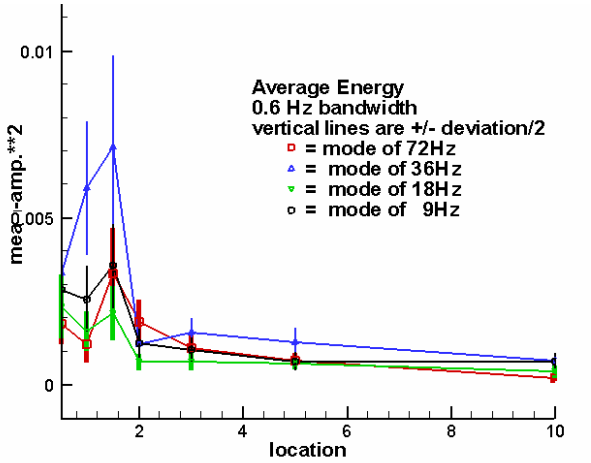

(26c)

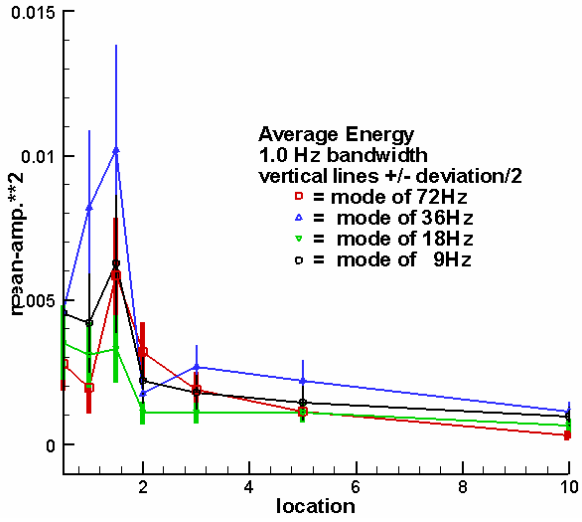

Fig.26 The estimated mean amplitude of different waveforms at different x locations: (a) uses a bandwidth of 0.3Hz; (b) uses 0.6Hz; and (c) uses 1Hz.

(27a)

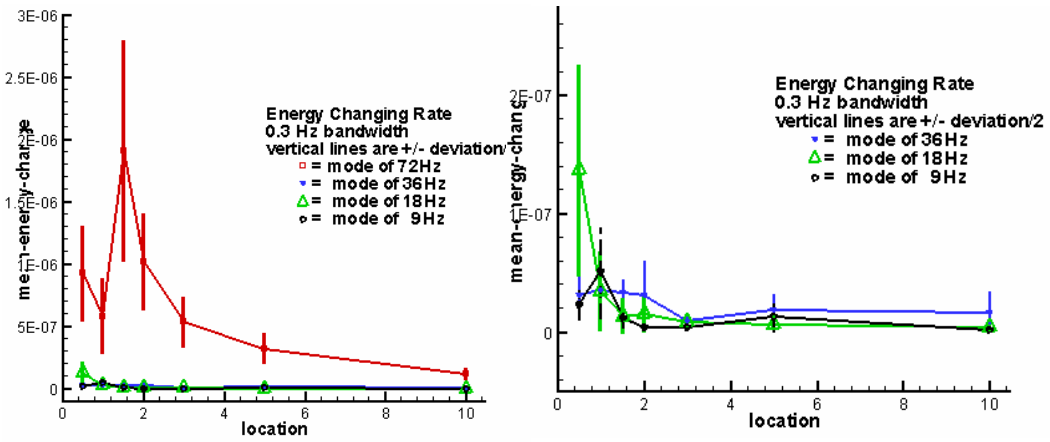

(27b)

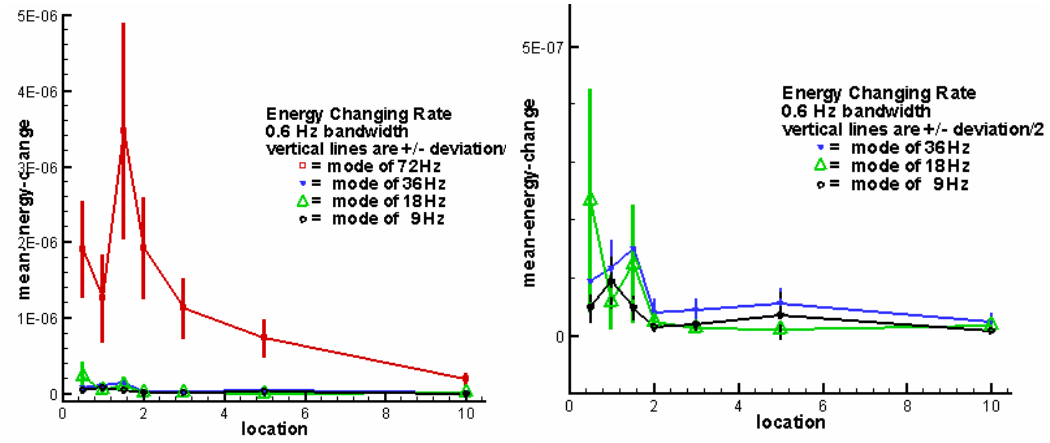

(27c)

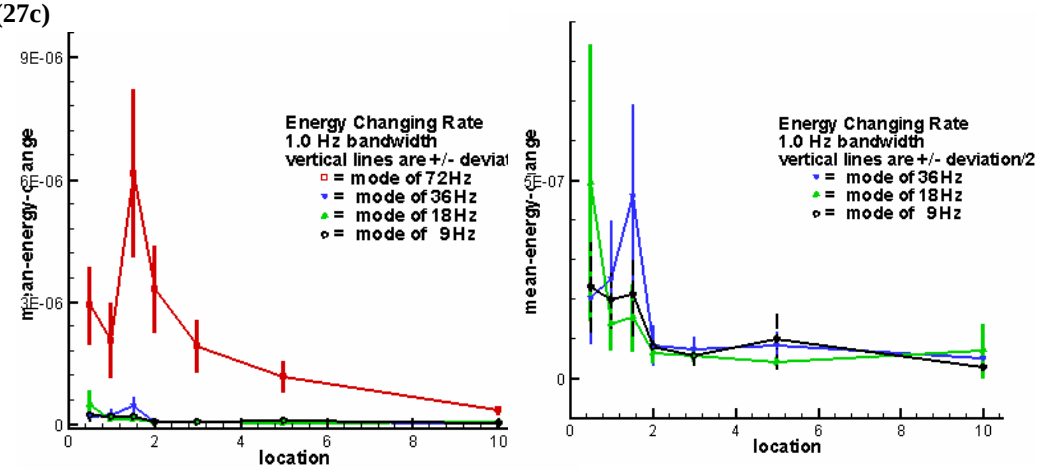

Fig.27 The estimated mean energy changing rates of different waveforms at different x locations, left figures are overall plots and right figures are detailed plots: (a) uses a bandwidth of 036Hz; (b) uses 0.6Hz; and (c) uses 1Hz.

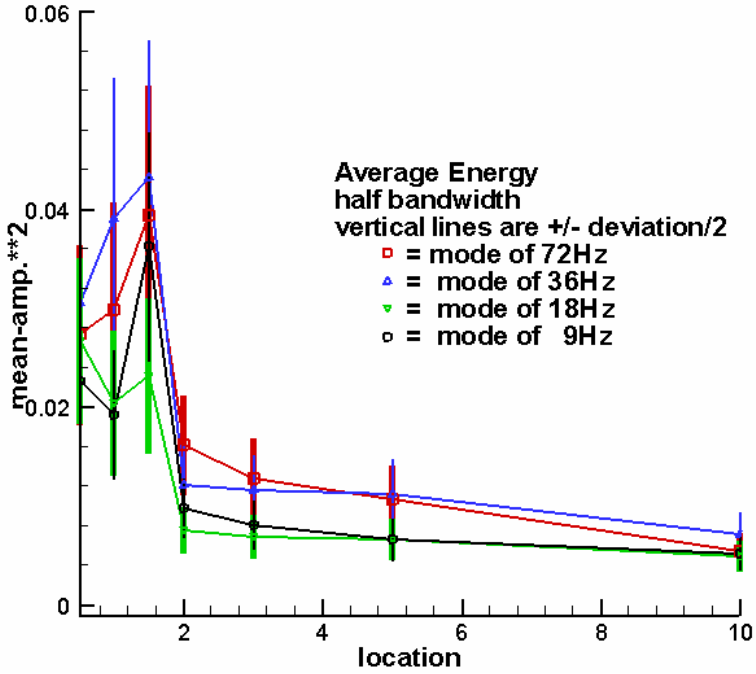

Fig.28 The comparison of the average energy measures between different wide bandwidth waveforms, these modes use 4.5-13.5Hz, 13.5-27Hz, 27-54Hz, and 54-108Hz windows, respectively.

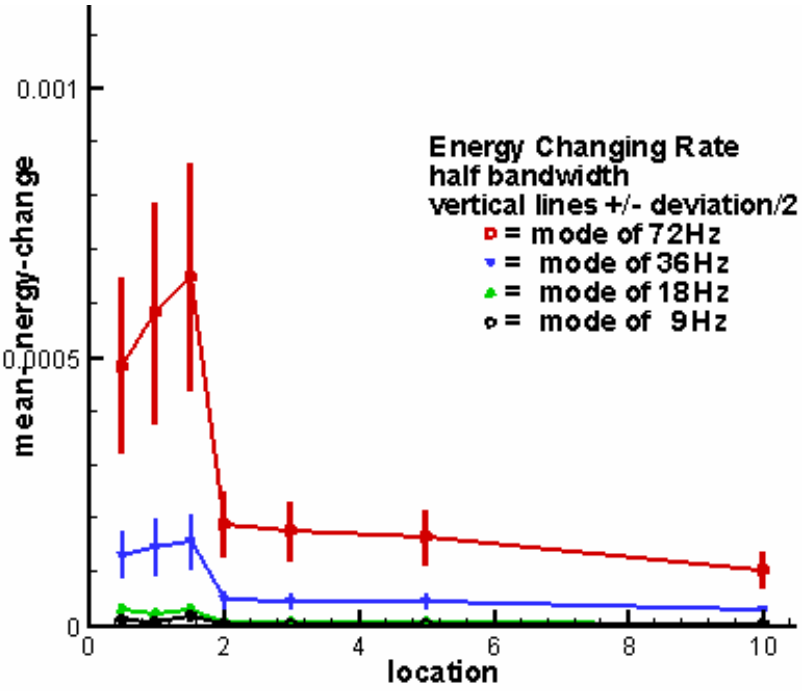

Fig.29 The comparison of the average energy changing rates between different wide bandwidth waveforms, these modes use 4.5-13.5Hz, 13.5-27Hz, 27-54Hz, and 54-108Hz, respectively.